Rarefied Gases and Functionalized Surfaces

Vom Fachbereich Produktionstechnik
der

UNIVERSITÄT BREMEN

zur Erlangung des Grades
Doktor der Ingenieurwissenschaften (Dr.-Ing.)
genehmigte

DISSERTATION

von
M.Sc. Simon KUNZE

Gutachter: Prof. Dr.-Ing. Jorg THÖMING
Prof. Dr. rer. nat. Marc AVILA

Tag der mündlichen Prüfung: 23.08.2023

CHEMISCHE VERFAHRENS-TECHNIK

Universität Bremen

"Essentially, all models are wrong, but some are useful."

George E. P. Box, Norman R. Draper

Abstract

Flow behavior of rarefied gases and their interactions with surfaces is of great interest in scientific fields like catalysis, gas separation membranes and space technology. To describe such gas flows, expensive numerical simulations are often needed. Simple, analytical models either cover very special cases or need empirical parameters, reducing their predictive power. These numerical as well as analytical modeling approaches are mostly concerned with simple surfaces. In gas separation membranes, however, surfaces are often treated with functional molecules, altering the interaction between gas and surface. Additionally, membranes have irregular geometries. Therefore, using a defined geometry like a straight channel allows focusing on the underlying effects. In this work, an analytical model is developed to describe rarefied gas flow in straight channels for all rarefaction regimes. Experimental flow data using plain and functionalized channels is acquired and compared to the model. The combination of the model and experimental results helps to interpret phenomena involved in rarefied gas flow in an intuitive way and sheds light on general aspects of gas-surface interactions of rarefied gases.

Zusammenfassung

Das Strömungsverhalten von verdünnten Gasen und ihre Interaktion mit Oberflächen ist von großer Bedeutung unter anderem für Katalyseforschung, Gastrennungsmembranen und Weltraumtechnik. Um solche Strömungen zu beschreiben sind häufig aufwendige, numerische Berechnungen notwendig. Einfache, analytische Modelle haben entweder einen sehr eingeschränkten Gültigkeitsbereich oder benötigen empirische Parameter, die die Übertragbarkeit des Modells auf unbekannte Situationen schmälern. Diese numerischen als auch analytischen Modelle beschäftigen sich hauptsächlich mit einfachen Oberflächen. In Gastrennungsmembranen werden Oberflächen jedoch häufig mit funktionalen Molekülen behandelt, die die Interaktion zwischen Gas und Oberfläche verändern. Membranen haben zudem eine irreguläre Struktur. Eine definierte Geometrie in Form eines geraden Kanals hilft dabei, sich auf die zugrundeliegenden Effekte zu konzentrieren. In dieser Arbeit wird ein analytisches Modell entwickelt, das in der Lage ist Gasströmungen über alle Verdünnungsbereiche in geraden Kanälen zu beschreiben. Es werden Gasströmungen in unbehandelten und funktionalisierten Kanälen experimentell untersucht und mit dem analytischen Modell verglichen. In Verbindung mit den experimentellen Daten erlaubt das Modell eine intuitive Interpretation der involvierten Phänomene und beleuchtet grundlegende Aspekte der Gas-Oberflächen-Interaktionen von verdünnten Gasen.

Acknowledgements

When I started with this project, I could not have imagined how much patience and perseverance would be required. There was more than once a moment where I was on the verge of throwing in the towel. Without the backup, assistance and moral support of many people, I would not have been able to successfully finish this venture. Whenever there was a rocky road with unpleasant headwind, I could be assured to have cover. When climbing a steep hill, I was being pushed forward, countering the urge to back off.

Thank you to my colleagues at the Chemical Process Engineering group at University Bremen, with whom I spent some nice years at work and beyond. Such a familial working atmosphere is not to be taken for granted. Thank you to Jorg Thöming and Michael Baune for enabling the follow-up funding. Thank you to Marc Avila for taking the role as a second reviewer. Thanks to Benjamin Besser for extending the part of the working group investigating this topic from one person to two persons and enriching my daily work with so many fruitful discussions, and thanks to Rodion Groll for joining this ensemble. Thank you to the teams at Karlsruhe Institute of Technology and at University Aix-Marseille for making it possible to perform experiments using their facilities, and to the team of Andreas Lüttge for providing access to their VSI instrument. Thanks to Ingmar Bösing and Jasper Giesler for proofreading this thesis. And thank you, Bella, for being a bastion of calm whenever there were rages of storm.

List of relevant publications

S. Kunze, P. Perrier, R. Groll, B. Besser, S. Varoutis, A. Lüttge, I. Graur, and J. Thöming. "Rarefied Gas Flow in Functionalized Microchannels" (2023). DOI: 10.48550/ARXIV.2301.12575.

S. Kunze, R. Groll, B. Besser, and J. Thöming. "Molecular Diameters of Rarefied Gases". *Scientific Reports* 12.1 (2022), p. 2057. DOI: 10.1038/s41598-022-05871-y.

R. Groll, S. Kunze, and B. Besser. "Correction of Second-Order Slip Condition for Higher Knudsen Numbers by Approximation of Free-Molecular Diffusion". *Physics of Fluids* 32.9 (2020), p. 092008. DOI: 10.1063/5.0021711.

B. Besser, S. Kunze, M. Wilhelm, K. Rezwan, and J. Thöming. "Surface Functionalization of Mesoporous Membranes: Impact on Pore Structure and Gas Flow Mechanisms". *ACS Applied Materials & Interfaces* 12.35 (2020), pp. 39388-39396. DOI: 10.1021/acsami.0c08619.

Contents

List of Figures

List of Tables

List of Abbreviations

CVD	**C**hemical **V**apor **D**eposition
FM	**F**ree **M**olecular
HDTMS	**H**exa**d**ecyl**tri****m**ethoxy**s**ilane
TMAC	**T**angential **M**omentum **A**ccommodation **C**oefficient
VSI	**V**ertical **S**canning **I**nterferometry

Physical Constants

Ideal Gas Constant	$R = 8.314\,462\,618\,153\,24\,\mathrm{J\,K^{-1}\,mol^{-1}}$ (exact)
Boltzmann Constant	$k_B = 1.380\,649 \times 10^{-23}\,\mathrm{J\,K^{-1}}$ (exact)

List of Symbols

a	distance	m
b	adsorption affinity	-
c	concentration	$\mathrm{mol\,m^{-3}}$
d	molecular diameter	m
D	diameter of a channel	m
D_{AA}	self diffusion coefficient	$\mathrm{m^2\,s^{-1}}$
D_s	surface diffusion coefficient	$\mathrm{m^2\,s^{-1}}$
h	height of a channel	m
J_s	surface diffusion flux	$\mathrm{mol\,m^{-2}\,s^{-1}}$
L	length of a channel	m
L_C	characteristic length of a geometry	
	— D for circular, h for rectangular channels	m
M	molar mass	$\mathrm{kg\,mol^{-1}}$
Kn	Knudsen number	-
p	pressure	Pa ($\mathrm{kg\,m^{-1}\,s^{-2}}$)
T	temperature	K
$\mathbf{v}$	velocity (vector)	$\mathrm{m\,s^{-1}}$
u	velocity (scalar)	$\mathrm{m\,s^{-1}}$
w	width of a channel	m
ϵ_{LJ}	depth of the LJ potential well	m
λ	mean free path	m
σ	TMAC	-
σ_{LJ}	distance where the LJ potential is zero	m
Θ	fractional occupancy of the adsorption sites	-
μ	dynamic viscosity	$\mathrm{kg\,m^{-1}\,s^{-1}}$
Π	circumference of the channel	m

Indices

x_1	inlet (upstream)
x_2	outlet (downstream)
x_m	mean

x_s	surface
x^*	value at t=0

Chapter 1

Introduction

The term *rarefied* refers to a state where a gas behaves different to what is expected when considering it as a continuum instead of as a collection of discrete particles. The continuum assumption is valid in many common situations but breaks down at particularly low pressures, like in space and vacuum technology, or in very small geometries, like in membranes and catalysts. A key parameter to quantify rarefaction is the Knudsen number, which is defined as the ratio of the mean free path of the gas and the characteristic length of the surrounding geometry. For example, this characteristic length would be the pore diameter in porous media. The mean free path is the mean distance a gas molecule is free to travel without colliding into another molecule. The Knudsen number therefore gets larger for increasing rarefaction. Rarefied gases are relevant to many technical applications and scientific fields, like catalysis [1], space technologies [2], gas separation membranes [3] and micro-electro-mechanical systems [4]. A more detailed overview about rarefied gases and the corresponding phenomena is given in chapter 2.

An important range of rarefaction is the transition regime around Knudsen = 1, see figure 1.1a. This regime is particularly interesting because a major challenge regarding rarefied gases is the fact that there is no simple, analytical and predictive model to describe the flow even in simple geometries for all Knudsen numbers including the transition regime. However, such a model is desirable to avoid costly numerical computations or experiments. Chapter 3 of this work gives an overview on existing modelling approaches and introduces an analytical model capable of predicting flows for all degrees of rarefaction in simple geometries using an intuitive approach.

As mentioned above, an important technical application of rarefied gases are gas separation membranes. These membranes are modified using molecules which are attached to the inner membrane surface, see figure 1.1b. This process is called *functionalization*. Such modification enables membranes to selectively interact with specific gases. For membrane design, it is

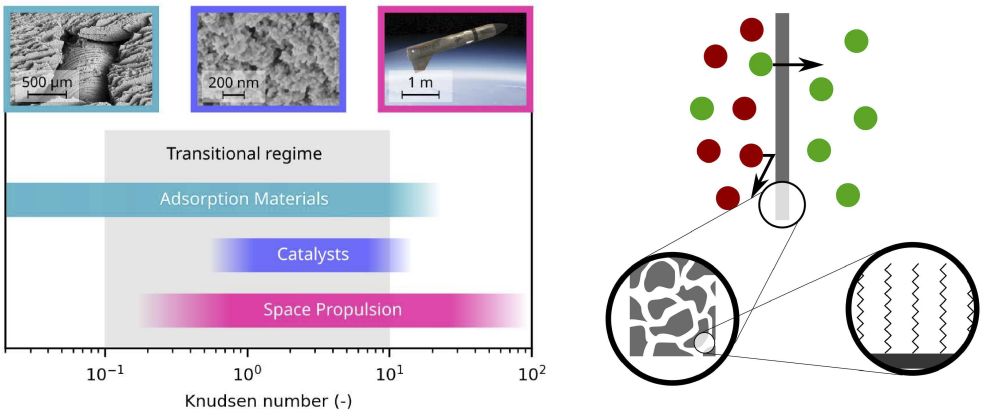

(a) (b)

Figure 1.1: **(a)**: Typical Knudsen regions of technical applications. Materials for gas adsorption (cyan) can have pore sizes ranging over multiple orders of magnitude. In combination with large changes in pressure or temperature in swing adsorption applications, the result is a wide Knudsen range. In catalysis (blue), products and educts often face small structures at high temperatures and Knudsen numbers larger than unity at atmospheric pressure can be observed. In space applications such as propulsion modules (magenta), the Knudsen numbers tend to be very large due to the low pressure in orbit. Left image: SEM image of a hierarchical structured zeolite adsorbent. Center image: SEM image of a Sm_2O_3 xerogel catalyst. Right image: Depiction of the ReFEx vehicle [5]. See A.1 for details on the calculation of the Knudsen numbers. Figure and description adapted from [6]. **(b)**: A schematical depiction of a gas separation process, the inner structure of a membrane and its functionalization.

important to understand the mechanisms of gas-membrane interactions. To study these interactions and to exclude effects resulting from the irregularity of porous media, an idealized geometry in form of a straight channel is used in this work. Chapter 4 focuses on the acquisition and analysis of experimental data of rarefied gas flow in plain and functionalized straight channels and the comparison with the analytical model introduced before.

The overall goal of this thesis is to set the foundation for a simple, analytical description of rarefied gases, which can potentially be extended to more complex geometries and thus significantly reduce the computational cost related to the description of such gas flows. The model uses the molecular diameter of a gas as a parameter which is determined using experimental data. The model is then applicable without further modification to unknown cases. The combination of the model and experimental data sheds light on

the importance of the scale of the surrounding geometry when considering surface effects and allows general insight into gas-surface interactions of rarefied gases.

Chapter 2

Rarefaction phenomena

This chapter provides an overview on rarefied gases and associated phenomena, focusing on surface interactions which are crucial for modeling the gas flow and interpreting experimental results.

The mean free path λ describes the average distance a gas molecule can travel without colliding with another one. The mean free path of a molecule can be calculated using its viscosity [7] by

$$\lambda_{visc} = \frac{\mu}{p}\sqrt{\frac{\pi RT}{2M}} \tag{2.1}$$

where μ is the dynamic viscosity, p is the pressure, R is the ideal gas constant, T is the temperature and M is the molar mass. λ can also be calculated using its molecular diameter d [8, p. 716] by

$$\lambda_d = \frac{k_b T}{\sqrt{2}\pi d^2 p} \tag{2.2}$$

where k_b is the Boltzmann constant.

Under many conditions, λ is very small compared to the surroundings and the gas can be treated as a continuum. This means that the gas is not considered as a collection of discrete particles, but as a continuous mass with macroscopic properties like pressure and temperature [8, p. 53]. However, when λ approaches the scale of the characteristic length L_C of the surrounding geometry, the continuum hypothesis breaks down because an integral definition of pressure and temperature for a volume element is not reasonable anymore [9, pp. 15f]. In this case, gas flow cannot be described with models based on that hypothesis. The characteristic length is dependent on the geometry – in this work, it is the diameter for circular channels and the

height for rectangular channels. The ratio of mean free path to the characteristic length L_C is called *Knudsen number* Kn

$$\mathrm{Kn} = \frac{\lambda}{L_c} \tag{2.3}$$

and divides the flow regimes into typical areas of *viscous flow* ($\mathrm{Kn} < 10^{-3}$), where the continuum hypothesis is valid, *slip flow* ($10^{-3} < \mathrm{Kn} < 0.1$) and *transition flow* ($0.1 < \mathrm{Kn} < 10$), where rarefaction effects have significant impact, and *free molecular flow* (FM) ($\mathrm{Kn} > 10$), where the intermolecular interaction becomes negligible [10].

2.1 A brief history

An analytical description of gas flow dates back to 1840, where the so-called Hagen-Poiseuille law was published [11] which is suitable to calculate continuum gas flow in circular channels and was later adapted to other geometries. The first mathematical foundation to describe the chaotic nature of gas molecules statistically was set by Ludwig Boltzmann, who published the most important parts of his work 1896 in *Vorlesungen über Gastheorie* [12, 13], which was later translated to English [14]. Boltzmann introduced the concept of the probability density function $f(t, r, c)$ which describes the number density of molecules at time t, position r and absolute molecular velocity c [15] and which is defined by the Boltzmann equation. One of the formulations [16, pp. 67, 72] reads

$$\frac{\partial f}{\partial t} + c\frac{\partial f}{\partial r} = Q(f, f) \tag{2.4}$$

where $Q(f, f)$ is the collision operator describing the interaction between two molecules. This collision operator makes the Boltzmann equation inherently hard to solve [16, p. 95]. A popular choice for modeling the collision operator is the Bhatnagar-Gross-Krook (BGK) model introduced in 1954 [17], which describes the magnitude of the collision proportionally to the deviation of f from a Maxwellian distribution [16, p. 95], which in turn describes a gas in its equilibrium.

Because of the invalidity of continuum models like the Hagen-Poiseuille and Navier-Stokes equations for rarefied gases, a closed-form expression

covering all Knudsen numbers has been addressed by many researches. Martin Knudsen, after whom the Knudsen number was named, described rarefied gas flow 1909 using interpolation between continuum and free molecular flow [18]. His expression for the free molecular regime, originally stated to be valid for all cross-sectional shapes, was then corrected 1910 by Marian Smoluchowski [19], who presented an expression describing free molecular flow in arbitrary cross-sections for different gas-surface interactions and showed that Knudsen's original expression was valid only for circular cross-sections. Clausing [20] extended 1932 what was only valid for very long channels to channels with arbitrary length. More recent approaches to describe the whole Knudsen range introduced parameters which are to be determined empirically and therefore lack predictive nature [21, 22, 23]. With available computational power, numerical methods became established [24, 25, 26, 27].

While the before-mentioned works are mainly concerned with low-pressure flows in larger geometries, work on micro flows in micro-electro-mechanical systems began in the late 1980s [9, p. 24] with first experimental results with micro-machined channels acquired in the 1990s [28, 29]. While basic experimental investigations regarding the diffusion of gases through various materials have been conducted by Thomas Graham in 1866 [30], gas separation processes using membranes became of industrial relevance in the 1980s [3, pp. 325f], involving rarefaction effects in their nano- and mesoporous structures. The functionalization of gas separation membranes, which aims to increase selectivity, introduce a surface interaction effect which is still not completely understood today [31].

2.2 Surface phenomena

When a gas is confined by solid matter, gas molecules inevitably interact with the solid surface. In the case of viscous flow, this interaction is macroscopically modeled by a no-slip boundary condition: the velocity of the gas becomes zero directly at the surface. Using this boundary condition, it is possible to derive simple analytical expressions for the Navier-Stokes equations for special cases.

At the molecular level, however, the interaction between gas and surface atoms is more complex. While the reflection of molecules can be characterized using the tangential momentum accommodation coefficient, additional effects like surface diffusion arise.

2.2.1 TMAC

When a molecule hits a wall with a tangential velocity, part or all of the tangential momentum is absorbed by the wall, which macroscopically manifests as the before-mentioned no-slip boundary condition for viscous flow. The tangential momentum accommodation coefficient TMAC describes the ratio of diffuse to specular reflection [32]. A TMAC of 1 means fully diffusive reflection, a TMAC of 0 means fully specular reflection. The diffusive reflection can be modeled using the Maxwell reflection model [33]. The TMAC is usually extracted by fitting a first-order slip boundary condition model, see section 3.1.2, to rarefied gas flow data [34].

The TMAC is discussed controversially in the literature. While often values between 0.75 and 1 are statet [35, 36, 34, 37], correlations with the Knudsen number [38], the surface topology [38, 39] and temperature [40] have been observed.

The TMAC is important in modeling the slip boundary condition and the free molecular flow and is therefore a crucial parameter for the description of rarefied gases. The diversity of results for TMACs even for the same gas species poses a big challenge for generally valid calculations.

2.2.2 Surface diffusion

Surface diffusion is a process relevant for technical applications like catalysis and transport in porous media and membranes [41, 42, 43, 44] and can contribute to great extent to the total mass transport [45]. For rarefied gases, it is hypothesized that surface diffusion can have an influence even in microporous systems [46].

Surface diffusion can be described as a three-step process with adsorption, diffusion, desorption, while the adsorption and desorption can be combined in an adsorption isotherm [45] which describes the amount of adsorbed matter as a function of the non-adsorbed concentration. Typically, a fractional surface coverage $\Theta = c_s/c_s^{sat}$ is used, where c_s is the concentration adsorbed onto the surface and c_s^{sat} is the saturated surface concentration, the maximum concentration of the adsorbate. A popular way to describe Θ is the Langmuir isotherm [47]

$$\Theta = \frac{bc}{1 + bc} \tag{2.5}$$

where c is the bulk (non-adsorbed) concentration and b is the adsorption affinity. The surface diffusion flux J_s itself can be described by hopping mechanisms, hydrodynamic models or Fickian approaches like

$$J_s = -D_s \nabla c_s \tag{2.6}$$

where D_s is the surface diffusion coefficient [45].

2.2.3 Surface functionalization

By attaching molecules onto the surface and thus *functionalizing* it, the gas-surface interaction can be modified. This is applied to alter the selectivity of gas separation membranes [48, 49] or gas chromatography columns [50]. Polar functional groups like amino groups are used to capture carbon dioxide [49, 51]. It can be observed that applying such a surface functionalization significantly reduces the gas flow [52]. It was shown that in mesoporous media, the length of the functionalization molecule is the determining factor for the flow reduction even when taking into account the pore diameter reduction of the functional molecules, while the chemical composition of the functional group itself does not seem to have an influence [31]. To maximize an observable effect, the impact of the functionalization should be as large as possible. Therefore, a long C_{16} alkyl chain, Hexadecyltrimethoxysilane (HDTMS), is used in this work for surface functionalization of the microchannels.

Chapter 3

Analytical modeling of rarefied gas flow[1]

This chapter introduces an analytical model describing rarefied gas flow for all Knudsen numbers. The involved mechanisms and related concepts are introduced in section 3.1 together with other typical modeling approaches found in literature. An attempt to adapt an existing superposition model is described in section 3.2. This model fails to generalize for different geometries but clarifies the importance of geometric scale when considering surface diffusion-like effects. The actual model capable of predicting rarefied gas flow in straight channels for arbitrary geometric scales is developed in section 3.3.

3.1 Theoretical background

3.1.1 Molecular diameters

In many natural processes and technical applications, the size of a gas molecule is a key property. Since it is also crucial for the analytical model introduced in section 3.3, an overview about different definitions of molecular diameters is given here.

Molecular diameters influence the rate at which lungs can absorb oxygen [53], affect chemical reactions [54], define the drag on wind turbines [55] and limit diffusion across membranes [3], mainly because the size strongly affects the mobility of a molecule. For unification, the size is often generalized as the diameter of an equivalent sphere. However, a molecule is neither a rigid object nor has, in most cases, a spherical shape. Its volume is made up of electron orbitals representing the probability of finding an electron at a specific position. It is, therefore, impossible to state one definite diameter

[1] Parts of this chapter have been published verbatim in [6].

of a molecule. As a result, different operationally defined diameters are used for various scenarios.

The van der Waals diameter is a prominent measure and is typically used to calculate the properties of condensed matter [56]. The van der Waals diameter, see figure 3.1a, is obtained by crystallographic experiments such as X-ray diffraction, zero point density data [56] or the molar volume of solids [57]. This diameter is also applied in the van der Waals equation of state to account for the nonideal behavior of gases under high pressure [58, 59].

Transport processes such as the absorption of oxygen in the lungs or gas transport through a membrane are strongly influenced by diffusion effects. The diffusion coefficients of molecules can be estimated based on their diameter. Here, the kinetic diameter of a molecule is frequently used, which is obtained from molecular sieving experiments [3], see figure 3.1b.

The drag on wind turbines is mainly a result of gas viscosity. Viscosity is also an effect resulting from the molecular diameter of a gas. Measured viscosity, usually obtained at normal pressure, can therefore be used to estimate molecular diameters, see figure 3.1c, and to calculate the mean free path of a molecule, see equation 2.1.

None of these diameters explicitly correspond to rarefied conditions. This raises the question of the extent to which they are applicable for rarefied gases and whether there is a more suitable diameter. The analytical model introduced in this work will address this.

3.1.2 Slip flow

Slip flow is one of the transport mechanisms used in the analytical model introduced in this work. The derivation and different implementations are discussed in this section.

The convective flow, which is the mass flow due velocity forced by a pressure gradient [8, p. 132], is characterized by the continuum assumption. A common way to model convective flow is using the Navier-Stokes equations. A solution to the Navier-Stokes equations in a circular channel is the Hagen-Poiseuille equation [8, p. 116]

$$\dot{m}_{HP}^{circ} = p_m \Delta p \frac{\pi D^4}{128 L} \frac{M}{\mu R T} \tag{3.1}$$

where $\dot{m}$ is the mass flow, $p_m = (p_1 + p_2)/2$ is the mean pressure, $\Delta p = p_2 - p_1$ is the pressure difference between upstream and downstream, D is

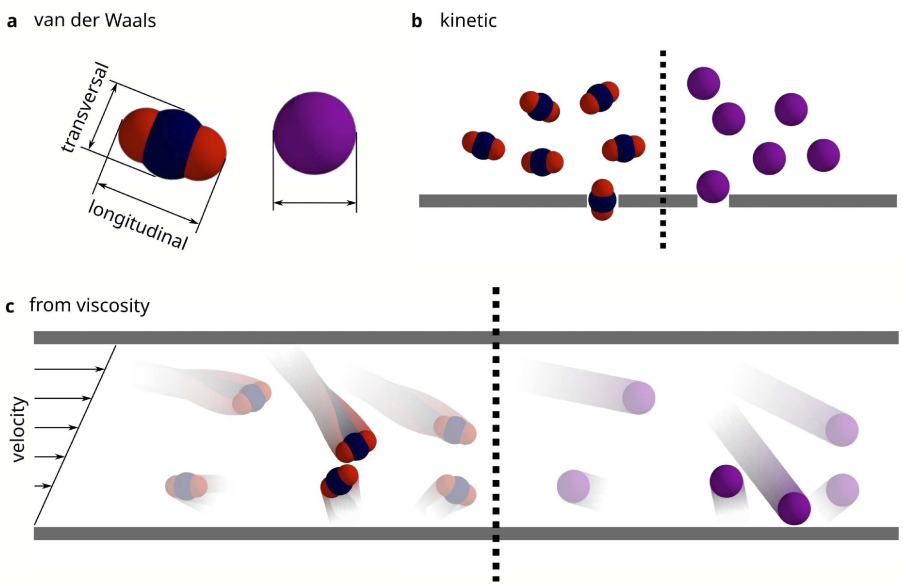

Figure 3.1: Visualization of different molecular diameters. **(a)** The van der Waals diameter has two definitions for an asymmetric molecule like carbon dioxide while a spherical gas like argon just has one. **(b)** Molecular sieve experiments yield the kinetic diameter [3]. Molecular shape can have a large influence on the result. Here, carbon dioxide can pass the sieve in the right orientation, while argon is too large. This results in a larger kinetic diameter for argon than for carbon dioxide. **(c)** Viscosity (ν) can be measured by the momentum exchange from one moving boundary to a stationary one. The momentum exchanges through diffusion from fast moving molecules (top) to slow moving molecules (bottom). This diffusion is limited by the mean free path. While the two highlighted carbon dioxide molecules collide because of their size, the argon molecules can pass. The larger the molecules, the slower the molecules can diffuse, resulting in lower measured viscosity [60]. This results in a larger viscous diameter for carbon dioxide than for argon.

the channel diameter, and L is the channel length. A solution can also be derived for rectangular channels [61] and results in

$$\dot{m}_{HP}^{rect} = \frac{wh^3}{16L}\frac{M}{\mu RT}\frac{p_1^2 - p_2^2}{2}\frac{4}{3}\left(1 - \frac{192}{\pi^5}\left(\frac{h}{w}\right)\sum_{n=1,3,5\ldots}^{\infty}\frac{1}{n^5}\tanh\left(\frac{n\pi}{2}\frac{w}{h}\right)\right) \tag{3.2}$$

where w is the channel width and h is the channel height.

However, the continuum assumption is only valid if the Knudsen number is close to zero. When this is not the case anymore, rarefaction effects begin to play a role and the Hagen-Poiseuille equation can not be used in its classical form. To account for rarefaction effects near the surface, Maxwell

[33] proposed a boundary condition which results for round channels in

$$u_s^{circ} = -\alpha\lambda \left.\frac{du}{dr}\right|_{r=D/2} = -\alpha\frac{\lambda D}{4\mu}\frac{dp}{dx} = \alpha\frac{\lambda D}{4\mu}\frac{\Delta p}{L} \tag{3.3}$$

where u_s is the velocity difference between the wall and the gas directly at the wall. du/dr is the directional derivative of the gas velocity normal to the wall. λ is the mean free path of the gas and depends on the molecular diameter via equation 2.2, and α is expressed as:

$$\alpha = \frac{2-\sigma}{\sigma} \tag{3.4}$$

where σ is the TMAC, see section 2.2.1. This introduces a velocity offset at the boundary in contrast to the classical zero velocity boundary condition, and is therefore called slip boundary condition. An intuitive explanation of the dependence of equation (3.3) on λ is that near the surface the macroscopic velocity is the mean of the velocities of the molecules coming from the bulk and the molecules coming from the surface. The molecules coming from the bulk have the velocity of the place where they encountered their last collision, this is around λ away from the surface [15, p. 204]. The velocity there is defined by the velocity gradient $\frac{du}{dr}$ at the surface.

The resulting flow due to the slip is the density-weighted slip velocity over the cross-section:

$$\begin{aligned} \dot{m}_S^{circ} &= \rho u_s^{circ}\frac{\pi}{4}D^2 && (3.5)\\ &= p_m\frac{M}{RT}u_s^{circ}\frac{\pi}{4}D^2 && (3.6)\\ &= p_m\Delta p\frac{\pi D^3}{16L}\frac{M}{\mu RT}\alpha\lambda && (3.7) \end{aligned}$$

The overall convective flow is the sum of the plain Hagen-Poiseuille flow, see equation 3.1, and the flow due to slip:

$$\begin{aligned} \dot{m}_C^{circ} &= \dot{m}_{HP}^{circ} + \dot{m}_S^{circ}\\ &= p_m\Delta p\frac{\pi D^4}{128L}\frac{M}{\mu RT} + p_m\Delta p\frac{\pi D^3}{16L}\frac{M}{\mu RT}\alpha\lambda\\ &= \dot{m}_{HP}^{circ}\left(1 + 8\alpha\frac{\lambda}{D}\right) && (3.8) \end{aligned}$$

For a rectangular channel, equation 3.2 can be augmented with the slip boundary condition [61] and results in

$$\dot{m}_C^{rect} = \dot{m}_{HP}^{rect} + \frac{wh^3}{16L}\frac{M}{\mu RT}(p_1 - p_2)\frac{2-\sigma}{\sigma}\mathrm{Kn}_2 p_2 \left[\frac{32}{3}\left(1 - \frac{192}{\pi^5}\left(\frac{h}{w}\right)\sum_{n=1,3,5\ldots}^{\infty}\frac{1}{n^5}\tanh\left(\frac{n\pi}{2}\frac{w}{h}\right)\right) - \frac{256}{\pi^4}\left(1 - \frac{h}{w}\right)\sum_{n=1,3,5\ldots}^{\infty}\frac{1}{n^4}\tanh^2\left(\frac{n\pi}{2}\frac{w}{h}\right)\right]. \tag{3.9}$$

To extend the validity of the Navier-Stokes equations for higher Knudsen numbers, second order and higher order slip expressions have been developed [9, pp. 66ff] introducing new empirical parameters. This makes a general applicability hard. Other approaches include quite phenomenological boundary conditions, e.g. [22], using three fitted parameters to adjust to the slip limit, the FM limit and transition regime using DSMC simulations. To maintain predictive power, the first order slip expression is used in the analytical model introduced in this work.

3.1.3 Diffusive flow

Diffusive flow is another transport mechanism considered in the analytical model introduced in section 3.3. Diffusion is the result of a concentration gradient striving towards an equilibrium by intermolecular collision. In the case of a single species A, this is the self-diffusion and can be modeled using Fick's first law [62]

$$J_{AA} = D_{AA}\frac{\partial c}{\partial x} \tag{3.10}$$

where J_{AA} is the molar flux, D_{AA} is the self-diffusion coefficient and $\frac{\partial c}{\partial x}$ is the concentration gradient along the channel which can be simplified as

$$\frac{\partial c}{\partial x} = \frac{\Delta c}{L} \tag{3.11}$$

when the gradient is assumed to be constant, where Δc is the difference between the concentration at the inlet and the outlet and L is the channel length. The concentration difference in turn can be expressed in terms of pressure as

$$\Delta c = \Delta p\frac{1}{RT} \tag{3.12}$$

where Δp is the pressure difference between inlet and outlet, R is the gas constant and T is the temperature.

The self-diffusion coefficient is influenced by the frequency of intermolecular collisions and therefore the mean free path λ together with the mean molecular velocity ν

$$\nu = \sqrt{\frac{8RT}{\pi M}} \tag{3.13}$$

resulting in

$$D_{AA} = \frac{1}{3}\lambda\nu. \tag{3.14}$$

The molar flux can then be used to calculate the mass flow by

$$\dot{m}_{D,AA} = MAJ_{AA} = \Delta p \frac{1}{3}\lambda\nu\frac{A}{L}\frac{M}{RT}. \tag{3.15}$$

3.1.4 Free molecular flow

For very high Knudsen numbers, the gas molecules basically do not interact with each other anymore and have straight trajectories from surface to surface. This is called the free molecular (FM) flow or regime. FM flow is considered as one transport mechanism in the analytical model introduced in section 3.3. The only interaction relevant for this regime is the one between gas molecules and the surface. This, again, can be described by the Maxwell reflection model, characterized by the TMAC. The flow itself can be described using an expression introduced by Smoluchowski [19]:

$$\dot{m}_{FM} = \alpha\frac{1}{2\sqrt{2\pi}}\sqrt{\frac{M}{RT}}\frac{\Delta p}{L}\Lambda \tag{3.16}$$

where α is defined by equation 3.4 and Λ is a geometry-dependent expression solvable numerically for arbitrary cross-sections. For circular cross-sections, the analytical solution is

$$\Lambda^{circ} = \frac{2D^3\pi}{3} \tag{3.17}$$

and for rectangular cross-sections it is

$$\begin{aligned}\Lambda^{rect} =& 2\left[h^2 w \ln\left(\frac{w}{h}+\sqrt{1+\left(\frac{w}{h}\right)^2}\right)\right.\\ &+ hw^2 \ln\left(\frac{h}{w}+\sqrt{1+\left(\frac{h}{w}\right)^2}\right)\\ &\left.- \frac{\left(h^2+w^2\right)^{3/2}}{3}+\frac{h^3+w^3}{3}\right].\end{aligned} \tag{3.18}$$

A combination of free molecular flow and slip flow, connected by an interpolation function, is given in [63].

3.1.5 Superposition of mass flow rates

The superposition of different mechanisms for the mass flow rate is an approach to account for the different phenomena present in different rarefaction regimes. This method is used for the analytical model introduced in this work incorporating slip flow, diffusive flow and free molecular flow. In the literature, superposition is also used in different ways to describe rarefied gas flow.

In [64], volume diffusion is combined with the Navier-Stokes equations resulting in good agreement for Knudsen up to 4. In [23], this approach is adapted by using an *effective volume diffusion* which takes into account the surrounding geometry for high Knudsen numbers and thus extends the model for high Knudsen numbers. However, three phenomenological parameters, each controlling the slip flow, the Knudsen minimum and the free molecular flow respectively, make the model hardly predictive.

In [65], convective flow without a slip boundary condition is combined with Fickian Diffusion to produce a model valid up to the beginning of the transition regime. An extension to this approach is given in [66] by adding surface diffusion, extending the model up to the free molecular regime. In [67], a second-order slip model is combined with free molecular flow to cover the whole Knudsen range.

3.1.6 Variable viscosity

A different approach not used for the analytical model introduced in this work is making the viscosity a function of the pressure which was proposed

in [64] to describe the mass flow rate for higher Knudsen numbers. This function consists of two empirical parameters which need fitting to experimental data. Using this viscosity, it is possible to extend the validity of the Navier-Stokes equations up to Knudsen numbers of 2 when combined with a second-order slip boundary condition. In [68], the viscosity is modeled with two empirical parameters covering the whole Knudsen range for circular and rectangular channels. A general investigation of the influence of rarefaction on the viscosity, denoted as *effective viscosity*, is given in [69] and phenomenologically explains the mass flow rate up to high Knudsen numbers.

3.1.7 Numerical methods

In this work, numerical models for calculating the mass flow rate are used for a comparison with the analytical model in addition to experimental data. The well-established Direct Simulation Monte Carlo (DSMC) method [24] can be used to calculate gas flows in accordance to the Boltzmann equation [70] by dividing the space into cells and simulating representative particles resembling the statistical behavior of a real gas. In contrast to DSMC, deterministic approaches include the linearized S-model equation [71] and the linearized Bhatnagar-Gross-Krook model equation which can be solved efficiently for simpler geometries like straight channels with circular, rectangular or trapezoidal cross-section [25, 72]. The Boltzmann equation itself can be solved in a linearized form as well [26, 27]. The analytical model introduced in section 3.3 will be compared to the linearized BGK model and the linearized S-model because of their efficiency for the given geometries.

3.1.8 Dimensionless mass flow

To visualize the whole Knudsen range and to exclude the influence of channel size, the mass flows are shown relative to a mass flow often called "Knudsen diffusion". This is the self-diffusive flow, see equation 3.15 with a mean free path equal to the hydraulic diameter $D_H = 4A/\Pi$, where A is the channel cross-sectional area, and Π is the perimeter of the cross-section. This mass flow recovers Knudsen's original expression for free molecular mass flow in circular channels [18, 73]. Normalizing yields the nondimensional mass flow:

$$G = \dot{m}\frac{3\Pi L}{8A^2\Delta p}\sqrt{\frac{\pi RT}{2M}} \tag{3.19}$$

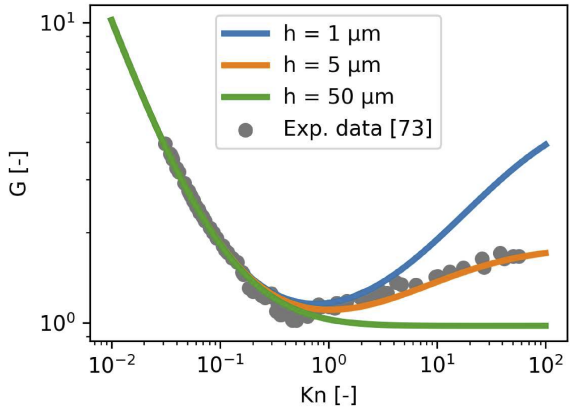

Figure 3.2: The solution of a superposed surface diffusion model for a rectangular channel with a width 30 times the height.

The actual mass flow decreases with larger Knudsen numbers. In the dimensionless representation, however, a typical phenomenon called Knudsen minimum [18] is clearly visible at approximately Kn = 1.

3.2 Preceding work

During the development of a model for describing rarefied gas flow, several options where evaluated. One of the more interesting and promising ones will be described here in more detail.

3.2.1 Scale variance of surface diffusion

When applying the superposed surface diffusion model introduced in [66] and fitting the surface diffusion parameters to experimental data, it works well for a single data set of a certain channel dimension. This can be seen in figure 3.2 where the orange line resembles the flow data in rectangular channels from [74]. Also, the Knudsen minimum mentioned in 3.1.8 is reproduced. The fitted parameters describe the surface diffusion in terms of surface interaction between the gas and the surface, so they are independent of the macroscopic dimension of the channel. This means that they should be the same for differently-sized channels when the channels have the same surface characteristics, which would make the model predictive in the first place.

The results of the model for different channel sizes with the same surface diffusion parameters is shown in figure 3.2. Smaller channels result in a

larger, larger channels in a smaller dimensionless mass flow G for high Knudsen numbers. However, according to theory, the shape of the dimensionless mass flow should be the same for different scales [68]. While it may be reasonable that very small structures have a higher influence of surface diffusion like discussed in 2.2.2, the example in figure 3.2 shows that for larger geometries, the Knudsen minimum vanishes completely, which is not in agreement with theory [68].

3.2.2 Surface concentration rise

Another problem with surface diffusion approaches is that the effects observed in rarefied gas flow experiments, particularly the rise of dimensionless mass flow after the transitional regime, occur also for inert gases like helium or argon. This is in conflict with a model attributing these effects to surface diffusion. Adsorption is the first step after which diffusion is possible. However, inert gases do not adsorb easily but would need high pressures to do so. Therefore, a dimensionless mass flow rise after the Knudsen minimum should not be observed for inert gases if this is attributed to surface diffusion.

Nevertheless, as observed in molecular dynamics simulations [75], gas generally tends to accumulate near solid walls due to the interaction forces between wall and gas molecules. The larger the Knudsen number, the higher the concentration at the surface compared to the bulk concentration. This is different from adsorption, because the gas does not stick to the walls but is only statistically more abundant near the walls. This effect is arguably very subtle, but can be used to model the same effects as in the surface diffusion approach.

Lennard-Jones potential

In classical molecular dynamics, interaction between molecules is often modeled by a force resulting from the Lennard-Jones potential [76]

$$V_{LJ} = 4\epsilon_{LJ}\left[\left(\frac{\sigma_{LJ}}{r}\right)^{12} - \left(\frac{\sigma_{LJ}}{r}\right)^{6}\right] \tag{3.20}$$

where r is the distance between two interacting particles, ϵ_{LJ} is the depth of the potential well and σ_{LJ} is the distance where the potential is zero. ϵ_{LJ} and σ_{LJ} are parameters which need to be determined, e.g. using experimental data or *ab initio* simulations.

Model implementation

To calculate the actual concentration of gas molecules near the channel surface, a continuum approach is used. The force due to the Lennard-Jones potential acting on the molecules result in a velocity, also called "drift". Additionally, gas molecules diffuse along a concentration gradient. These two components can be simultaneously described using a steady-state convection-diffusion differential equation without source term and constant self-diffusion coefficient D_{AA} [77, pp. 75f]:

$$0 = D_{AA}\nabla^2 c - \nabla(\mathbf{v}c) \tag{3.21}$$

The left term of equation (3.21) is the diffusion, the right term is the convection. c is the concentration and $\mathbf{v}$ is the velocity, a *drift* resulting from the force acting on the particles:

$$\mathbf{v} = \nabla V_{LJ} \tag{3.22}$$

While normally the drift velocity is calculated using the mobility as a proportionality factor, this factor can be skipped because V_{LJ} is already calculated using the free parameter ϵ which in turn is a proportionality factor for $\mathbf{v}$.

The force, modeled by the Lennard-Jones potential, would result in an accumulation of gas near the surface independently of the Knudsen number. The additional effect arising from a higher surface concentration, however, should only be significant for higher Knudsen numbers, thus resulting in an increased mass flow. To account for the fact that this effect does not occur at smaller Knudsen numbers, a quite phenomenological approach is used: the higher the concentration of molecules, the more they shield the potential of the surface from expanding into the bulk. This results in a smaller concentration rise for smaller Knudsen numbers, which matches the observations in [75]. For small Knudsen numbers, the shielding gets so large that the surface concentration rise becomes negligible.

The shielding is implemented in an iterative manner: the convection-diffusion equation is solved using an initial shielding strength. The shielding at position a is calculated by integrating the concentration c towards the wall, beginning at the center of the system at r and ending at a. This is then multiplied with the shield factor S, which in turn is a free parameter:

$$F_a = S \int_r^a c \, \mathrm{d}x \tag{3.23}$$

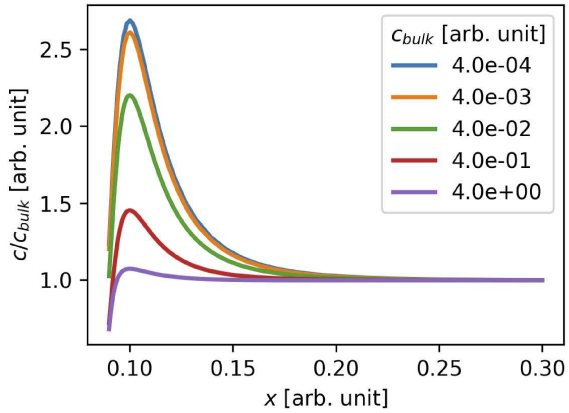

Figure 3.3: Relative surface concentration rise due to a Lennard-Jones potential and concentration-dependend shielding.

The new shielding field is then combined the shielding field of the previous iteration via a relaxation step using the relaxation factor α:

$$F_{a,relaxed} = \alpha F_{a,previous} + (1 - \alpha) F_a \tag{3.24}$$

The relaxed shielding is then applied to the original drift field from equation 3.22 to yield the shielded drift field:

$$\mathbf{v}_{shielded} = \mathbf{v}_{unshielded} / (1 + F_{a,relaxed}). \tag{3.25}$$

The shielded drift field is then used to recalculate equations (3.21)-(3.25) until convergence is achieved:

$$\text{error} = \text{abs}\left(\frac{\max(F_{a,relaxed}) - \max(F_{a,previous})}{\max(F_{a,relaxed})} \right) \tag{3.26}$$

In summary, there are three free parameters to fit this model: ϵ, denoting the strength of the interaction between the wall and gas molecules; σ, describing the range of these interactions; and S, the strength of the shielding effect which depends on the particle concentration and therefore the pressure in the system.

The shielding effect results in a lower relative concentration rise for higher pressures, which can be seen in figure 3.3.

The maximum concentration is then applied to the surface diffusion model described in [66]. Instead of using the bulk pressure for the adsorption isotherm, the elevated pressure near the surface is used.

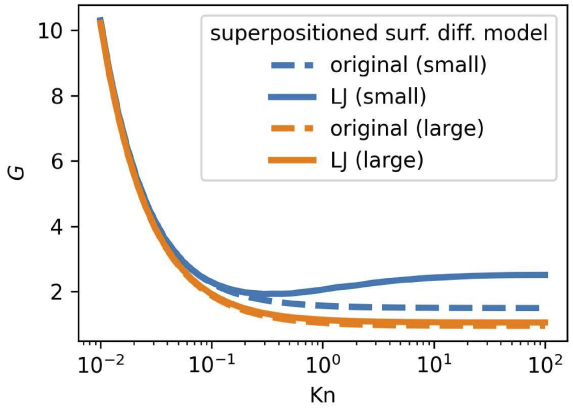

Figure 3.4: Dimensionless mass flow of the original superposed surface diffusion model and the modification using a Lennard-Jones (LJ) potential for two different channel geometries.

Scale variance of the model

As literature data shows [68] the characteristic dimensionless mass flow over the Knudsen number is the same for different channel sizes, excluding nanoporous systems. When a rise of gas concentration near the surface is responsible for this, the model derived above should work for arbitrary sized channels. This is not the case for a model with superimposed surface diffusion: the larger the channel, the smaller the surface-to-volume ratio and therefore the smaller the influence of any wall effect in form of a surface diffusion. This was shown in detail in section 3.2.1.

A surface concentration phenomenon could, however, compensate a lower surface-to-volume ratio in larger geometries because of an additional influence of the shielding, which is proportional to the gas density and weaker in larger geometries due to a lower pressure at the same Knudsen numbers. However, even when using this method, the result is strongly geometry-dependent, as seen in figure 3.4. Here, two different channel geometries are used. All other parameters of the model are the same for both cases. It is clearly visible that the surface diffusion model combined with the Lennard-Jones approach increases the mass flow for large Knudsen numbers due to the surface concentration rise, but this effect vanishes for larger geometries.

This shows that the same surface-to-volume relation as with the original surface diffusion approach is present. Therefore, the model does not explain the scaling-independent behavior of the dimensionless mass flow G and another modelling approach is required.

3.3 SED model

In this section, a fully predictive, analytical model for describing gas flow through straight channels for all Knudsen numbers is introduced and its implications in terms of molecular diameters and surface interactions are discussed.

Depending on the Knudsen number, it is to be expected that the fundamental equations for describing mass flow are different. Therefore, superposition of these effects is a reasonable approach. For the continuum and slip regime, gas can be modeled as a viscous flow using the Navier-Stokes equations, supplemented with a slip boundary condition. For the free molecular regime, the Smoluchowski expression can be used. To extend its validity to the transition regime, it is combined with self-diffusion, resulting in an *effective diffusion*. A superposition of these mechanisms results in the **s**lip **e**ffective **d**iffusion model, where the actual mass flow is just the sum of convective and effective diffusive flow:

$$\dot{m} = \dot{m}_C + \dot{m}_{D,eff}. \tag{3.27}$$

3.3.1 Effective mean free path and effective slip

The correction of a continuum model with a slip boundary condition is just an approximation and therefore only valid for slightly rarefied gases [15, pp. 5f]. As soon as the mean free path calculated from the density of the gas gets as large as the surrounding geometry, the walls begin to influence the actual mean free path. This was already stated by Bosanquet and described by Pollard and Present [78]: the free path of a gas molecule is either terminated by a collision with another gas molecule or with the wall. These collision frequencies can be added and are inversely proportional to the mean free path, which leads to an *effective mean free path*:

$$\lambda_{eff} = \left(\frac{1}{\lambda} + \frac{1}{L_c} \right)^{-1} \tag{3.28}$$

This effective mean free path can be substituted into equation (3.8):

$$\begin{aligned}\dot{m}_C^{circ} &= \dot{m}_{HP}\left[1+8\alpha\frac{\left(\frac{1}{\lambda}+\frac{1}{L_c}\right)^{-1}}{L_c}\right]\\ &= \dot{m}_{HP}\left[1+8\alpha\left(\frac{1}{Kn}+1\right)^{-1}\right]\\ &= \dot{m}_{HP}\left[1+8\alpha\frac{Kn}{1+Kn}\right]\end{aligned} \tag{3.29}$$

The effective mean free path can also be applied to the slip flow expression for rectangular channels by Jang *et al.* [61], see equation 3.9. Kn_2 in the original expression is replaced by $\frac{\lambda_{eff}}{h}\frac{p_m}{p_2} = \frac{Kn}{1+Kn}\frac{p_m}{p_2}$ to introduce the effective mean free path. Here, for the characteristic length, the height h of the channel is used. This results in the convective effective slip flow in rectangular channels:

$$\dot{m}_C^{rect} = \dot{m}_{HP}^{rect} + \frac{wh^3}{16L}\frac{M}{\mu RT}(p_1-p_2)\frac{2-\sigma}{\sigma}\frac{Kn}{1+Kn}p_m\left[...\right] \tag{3.30}$$

with the term in the squared brackets being the same as in equation 3.9, representing information about the width to height ratio of the channel.

3.3.2 Effective diffusion

Self-diffusion, see section 3.1.3, is generally used in non-rarefied conditions, where the surface does not have a significant influence on the behavior of the gas in terms of its mean free path. However, as soon as the Knudsen number approaches unity, this assumption does not hold. In the extreme of a free molecular flow, without any inter-molecular interaction, the gas flow can be described using an expression by Smoluchowski, see section 3.1.4.

To combine the two mechanisms of self-diffusive flow, see equation 3.15, and free molecular flow, see equation 3.16, an approach is introduced based the reasoning of Bosanquet which is described in the derivation of the effective mean free path above. This is reasonable because the diffusion coefficient is proportional to the mean free path [8] and the diffusive mass flows are proportional to the diffusion coefficients [77]. This yields an expression for the effective diffusive mass flow:

$$\dot{m}_{D,eff} = \left(\frac{1}{\dot{m}_{D,AA}}+\frac{1}{\dot{m}_{FM}}\right)^{-1} \tag{3.31}$$

3.3.3 Transition diameter

In the calculation of the effective mean free path, see equation 3.28, the classical mean free path is calculated using the molecular diameter, see equation 2.2. Therefore, the model has two free parameters: the TMAC and the molecular diameter.

Surfaces need to be extremely even to have specular reflection [39] and technical surfaces are likely to have diffuse reflection properties. This model assumes total diffuse reflection and therefore a TMAC of 1. In literature however, the TMAC for rectangular channels often resides around 0.9 [38]. This model therefore sets the TMAC just for the slip boundary condition for rectangular channels to 0.9, which results in good agreement with experimental and numerical data, with the emphasis that this is not actually a representation of a fractional specular reflection, but rather of an imperfect slip expression. The TMAC for the free molecular term is 1 in all cases.

Since the TMAC is fixed, the molecular diameter is left as the only free parameter. This parameter is used to extract what is called here *transition diameter* using literature data. After the determination of the transition diameter, which only needs to be done once for a certain gas, the model is fully predictive and can be applied without further modification to other geometries as shown further below.

For determination of the transition diameter, the free parameter of the model is fitted to the experimental data by least square optimization. The mass flow data is used in nondimensional form to avoid overweighting of high absolute mass flows for small Knudsen numbers. The prediction interval shown in figure 3.5 is calculated by

$$d \pm t_\alpha s \sqrt{1 + 1/N} \tag{3.32}$$

where s and N are the variance and number of data points, respectively. t_α is the percentile of Student's t-distribution corresponding to a confidence level of α [79]. In this case, $\alpha = 0.05$ is used for a two-sided 95 % confidence interval. The degree of freedom is $N - 1$ when fitting one parameter, the diameter in this case.

3.3.4 Knudsen number for plotting

The Knudsen number for plotting is calculated using the mean free path derived from the viscosity of the gas, see equation 2.1, instead of its diameter,

to ensure uniformity, implying that the experimental data shown is independent of the molecular diameter.

To compare two systems in a non-dimensional form, the de-dimensionalization must be applied in the same way for both systems. In this case, one system would be the experimental mass flows, the other system would be the analytical model with one of the diameters. The two important variables for comparison are the pressure of the system and the mass flow itself. The mass flow is uniformly de-dimensionalized using equation 3.19, where no ambiguity arises. To de-dimensionalize the pressure, the Knudsen number is used. However, the Knudsen number contains the mean free path and is therefore dependent on the molecular diameter.

To compare the experimental data with the model, the same de-dimensionalization of the pressure must be used, therefore the same Knudsen number and the same molecular diameter for calculating the mean free path is needed. Using the respective diameter for de-dimensionalization of each model version, for a meaningful comparison the experimental mass flows would need to use that diameter as well for de-dimensionalization. This would result in a mere x-axis shift. This x-axis shift would apply to both the model and the experimental data in the same way. Also, to avoid a cluttered plot, one would need to create a separate figure for each diameter, because all experimental data points would have slightly different positions for each diameter. To summarize, using the viscous diameter as an objective quantity allows to uniformly de-dimensionalize all experimental data and model results. Doing so differently would not change the determined sizes for a transition diameter.

3.3.5 Validation on literature data

The validation of the model is performed in two steps. In a first step, the transition diameter is determined using gas flow data in channels with circular cross-section. In a second step, the model is applied without further modification to rectangular channels. The data from literature is listed in table 3.1.

The data extraction from plots is done by using a software called WebPlotDigitizer [80] which is a very precise method because non-distorted images directly from the online versions of the papers were used. These plots often show a non-dimensional mass flow over the Knudsen number or something

similar. To get the raw experimental data from this, the pressure ratio p_r is used to acquire the inlet and outlet pressures via

$$p_2 = \frac{2p_m}{p_r + 1}, p_1 = p_2 p_r. \tag{3.33}$$

The mean pressure p_m in turn can be calculated from Kn. Fortunately, neither the plots because of the form of the dimensionless mass flow nor the method itself for determining molecular diameters is sensitive to the actual pressure ratio. Therefore, in the cases where assumptions had to be made, these assumptions are irrelevant to the result. Data of Knudsen [18] was truncated to suppress an over-weighted influence of the viscous regime, see table 3.1.

Table 3.1: Experimental data from literature used for the validation of the model.

Gas and source	**Extraction**	**Material and geometry**
He, N2, Ar [37]	from plot	Silica D = 49.6 µm L = 1.82 cm
N_2 [72]	raw data	Stainless steel D = 16 mm L = 1.277 m
CO_2, Röhre Nr. 4 [18]	raw data[2]	Glass D = 6.66 mm L = 2 cm
He [74]	raw data	Silica h = 9.38 µm; w = 492 µm L = 9.39 mm
He, N2, Ar [34]	from plot	Silica h = 9.38 µm; w = 492 µm L = 9.39 mm

The model is applied to the geometries of the experimental data using different molecular diameters: the diameter calculated from viscosity, the kinetic and van der Waals diameter. The latter can be defined in two ways for non-spherical molecules: the longitudinal and the transversal diameter. For nitrogen and carbon dioxide, the van der Waals diameters used here are derived from the van der Waals diameters found in literature for the elements

[2]Truncation of the first 8 data points of the viscous regime to focus the fit on the transition regime. No pressure ratio given; assumption of a ratio of 5.

as well as the binding length. For nitrogen, the transversal diameter is just the diameter of a nitrogen atom [81]. The longitudinal diameter is the diameter of one nitrogen atom plus the bond length between two nitrogen atoms which is 145 pm [60] since the bond length is defined from center to center. For carbon dioxide, the transversal diameter is just the diameter of a carbon atom, which is bigger than the oxygen atom. The longitudinal diameter is calculated by r(C) + bond(CO) + bond(OC) + r(C) which is equal to the diameter of a carbon atom plus two times the bond length between a carbon and an oxygen atom which is 116 pm [60]. The molecular diameters used here are summarized in table 3.2 and visualized in figure 3.5.

Table 3.2: Molecular diameters in pm.

Gas	**Transition (this work)**	**From viscosity** [60]	**Kinetic** [3]	**Van der Waals** [81, 60]
Helium	209 ± 3	215	260	286
Nitrogen	369 ± 9	370	364	477, 332
Argon	317 ± 3	358	340	366
Carbon dioxide	419 ± 8	453	330	586, 354

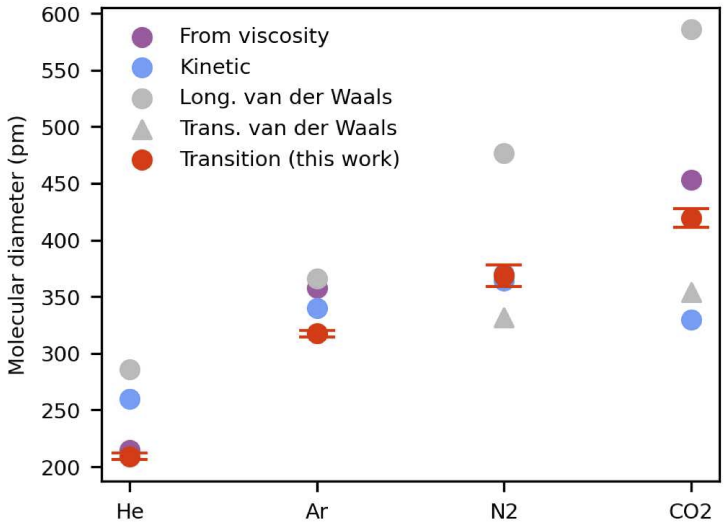

Figure 3.5: Compilation of molecular sizes. Error bars show the two-sided prediction interval of 95 %. The kinetic diameter of nitrogen and the diameter calculated from viscosity are covered by the transition diameter. The two van der Waals diameters for nitrogen and carbon dioxide are the transversal and the longitudinal ones.

Figure 3.6 shows the calculated mass flows together with the experimental results of gas flows through circular channels obtained from the literature for helium and argon [37], nitrogen [37, 72] and carbon dioxide [18]. For all diameters, the convective mass flow for $\mathrm{Kn} \to 0$ becomes identical, as in this range, the flow is dominated by the macroscopic property viscosity. Additionally, the free molecular mass flow for $\mathrm{Kn} \to \infty$ is equal because free molecular flow does not depend on molecular diameters but on the interaction with the geometry.

However, different diameters show distinct mass flows at approximately $\mathrm{Kn} = 1$ because here, the influence of slip is strong while the convective term is still present and self-diffusion is the dominating mechanism for diffusive flow. Both these terms are affected by the mean free path being in turn highly affected by the molecular diameter: the larger the molecule is, the smaller the mean free path. A smaller mean free path results in smaller diffusion and slip contributions and, therefore, in a smaller mass flow. This influence of molecular diameters is demonstrated by the mass flows resulting from the van der Waals diameters (in case of nitrogen and carbon dioxide, the longitudinal diameters), which are larger than the others (see figure 3.5), leading to a clearly overpronounced minimum at $\mathrm{Kn} = 1$. For argon, the deviation from data is less distinct. For the nonspherical molecules nitrogen and carbon dioxide, the smaller transversal diameter reproduces the data better than the larger longitudinal diameter. The kinetic diameter is neither the largest nor the smallest diameter. It is close to the van der Waals diameter for helium and thus also predicts a very distinct minimum. In contrast, the kinetic diameter of carbon dioxide is close to the small transversal van der Waals diameter and overpredicts experimental data. For argon, the kinetic diameter yields a slightly lower mass flow than the data, while it results in a good prediction for nitrogen.

The diameter calculated from viscosity gives reasonable results for helium and nitrogen. The mass flow for argon and carbon dioxide is slightly underestimated. Of all the literature diameters, this diameter seems to be the most suitable one even though showing deviations to experimental data.

Because of the predictive nature of the model, it can be applied to experimental data of mass flows using the molecular diameter as a free parameter, yielding a new type of diameter. Since the model is most sensitive in the transitional regime, we use the expression *transition diameter*. For the whole Knudsen range, the transition diameter-based model predicts the experimental mass flow data very well. Especially around the Knudsen minimum at

Kn = 1, the transition diameter shows superior agreement with experimental data compared to the literature values of the established molecular diameters. For Kn $\rightarrow$ 0, reasonable agreement with experimental data was expected because the main transport mechanism, convection, is influenced mainly by viscosity which is constant over pressure. The viscosity is taken from the literature data where the values are obtained under continuum conditions, rendering it a suitable property for describing gas flow under these conditions. In addition, the mass flow for Kn $\rightarrow \infty$ is convincingly predicted as a result of the dominating Smoluchowski expression in the free molecular regime, which is influenced only by the TMAC and the geometry of the channel and not by the molecular diameter, indicating that the TMAC is indeed unity for technical surfaces. A smaller TMAC would result in a higher mass flow for the free molecular regime, which is not represented by the experimental data. The good prediction for Kn = 1 is the result of the superposition of the different transport mechanisms at work. This agreement allows for the determination of a valid molecular diameter in this region.

Furthermore, the validity of the model can be confirmed by transferring it to rectangular cross-sections, as shown in figure 3.7. Here, transition diameter values obtained before are used as well as data for helium [34, 74] and for argon and nitrogen [34]. As discussed in section 3.3.3, the TMAC is set to 0.9 for the slip expression which provides good results. Since TMAC is defined as the ratio between diffuse and specular reflection, the values should be equal for surfaces with similar roughness made from a similar material. Apparently, the TMAC for the slip expression is also a function of cross-sectional shape, whose expression has not yet been established. To account for this cross-section effect, the TMAC in the slip expression is adjusted, while the TMAC for the free molecular flow is still unity. A clear indicator that the TMAC should in fact be unity for technical surfaces is the mass flow in the free molecular regime for Kn $\rightarrow \infty$, as discussed above. This contradiction could point to an imperfection in the slip expression for rectangular channels.

The well-known Knudsen minimum at Kn = 1 is properly predicted by the model. The minimum is more pronounced for high-ratio rectangular channels than for circular channels, which is a phenomenon widely known in the literature [68]. The reason for this phenomenon is the geometry-dependent behavior of free molecular flow as expressed by the Smoluchowski equation: the flow through an infinitesimal cross-sectional element is proportional to the mean of its distances to equiangular spaced points on

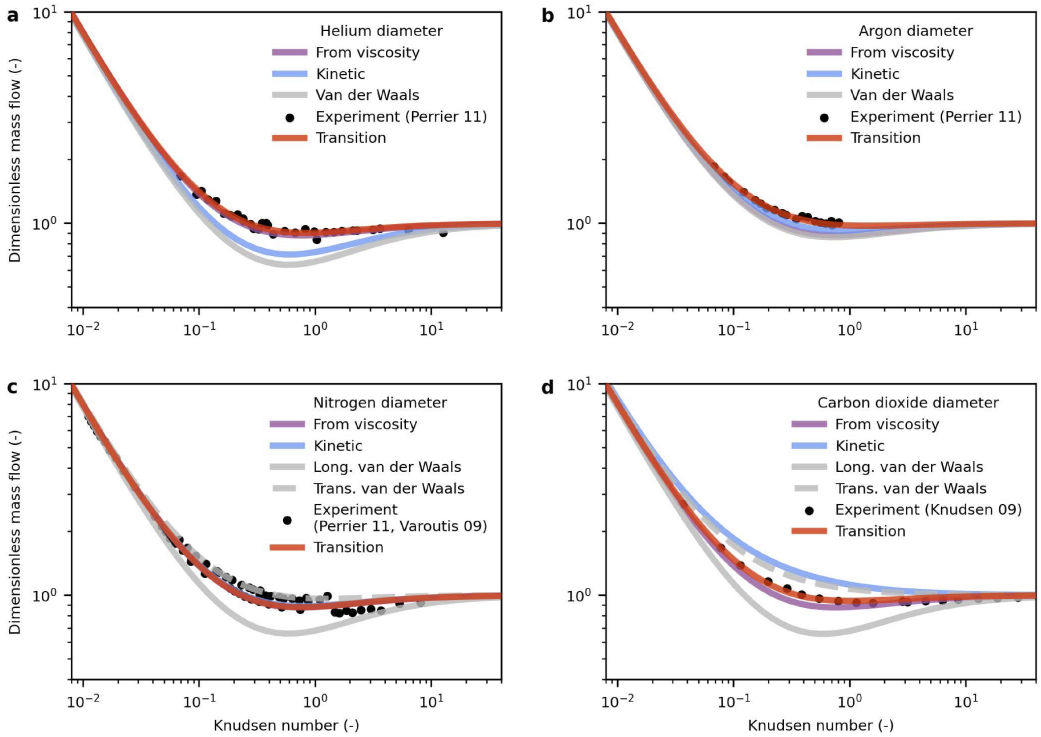

Figure 3.6: Mass flow in circular channels modelled with different molecular diameters compared to experimental data obtained from the literature. Dimensionless mass flow of **(a)** helium [37], **(b)** argon [37], **(c)** nitrogen [37, 72] and **(d)** carbon dioxide [18] predicted by the model. The transition diameter is determined by least squares fitting to equation 3.27. For comparison, the results for calculations using established molecular diameters from the literature are shown. For the nonspherical molecules nitrogen and carbon dioxide, two different van der Waals diameters are given for the transversal and longitudinal orientation, respectively.

the boundary at the element's axial position, since these distances are proportional to the distances molecules are free to travel. For rectangular channels, the sum of the mean distances of all cross-sectional elements is larger than the sum of the mean distances of a circular channel with equal hydraulic diameter and thus yields a larger nondimensional mass flow in the free molecular regime. This effect is the more enhanced the larger the channel's aspect ratio becomes. Although rectangular geometries are more intricate than circular geometries, the model represents the experimental data well with transition diameters, resulting in the best agreement with the data, demonstrating the predictive capability of the model with a known molecular diameter.

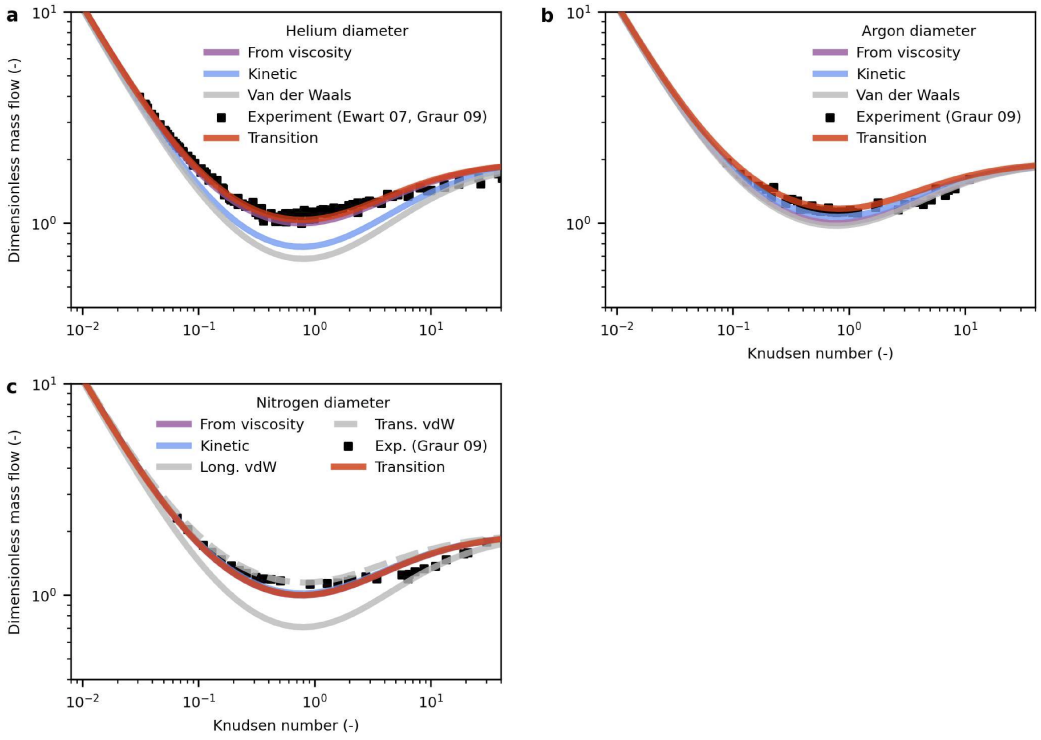

Figure 3.7: Mass flow in rectangular channels modelled with different molecular diameters compared to experimental data obtained from the literature. Dimensionless mass flow of **(a)** helium [74, 34], **(b)** argon [34] and **(c)** nitrogen [34] predicted by the model. The transition diameters are obtained from data on circular channels. For comparison, the results for different typical literature diameters are shown. For the nonspherical molecule nitrogen, two different van der Waals diameters are given for the transversal and longitudinal orientation, respectively.

Error analysis

To analyze the quality of the model, the deviations between the modelled mass flow and experimental data are investigated. For a model explaining the data well, these deviations should occur only due to noise in the measurement data. This is the case for the circular channels, as seen in figure 3.8: the deviations are scattered around zero for all Knudsen numbers. Carbon dioxide is an exception, but those deviations are small. For nitrogen, the systematic error originating from two different sources becomes apparent. The systematic deviations for the rectangular channels presumably result from measurement uncertainties of pressure sensors, as shown in figure 3.9. Although the deviations are scattered due to measurement noise, the distribution is not even around zero for all Knudsen numbers. For nitrogen and

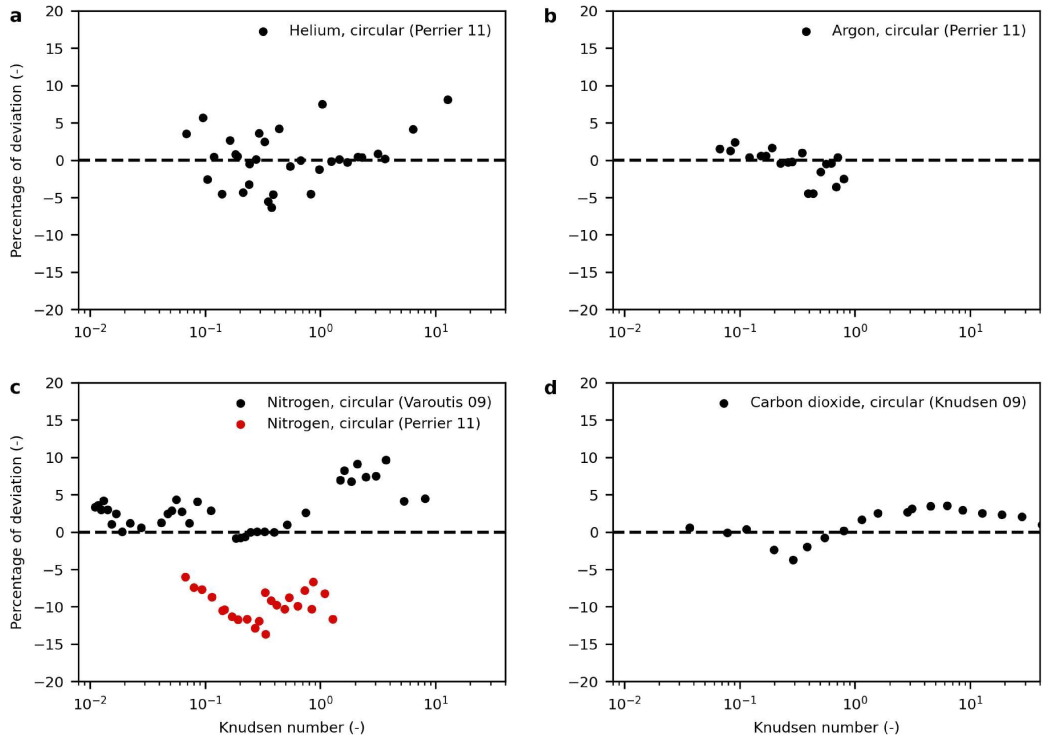

Figure 3.8: Deviation of modelled mass flow from experimental data for circular channels for **(a)** helium [37], **(b)** argon [37], **(c)** nitrogen [72, 37] and **(d)** carbon dioxide [18]. The deviation is scattered without any discernible pattern, except for carbon dioxide, a strong indicator that the proposed model explains the experimental data well.

helium in regions of Kn < 3, the modelled mass flow is smaller than the experimental data. For regions of Kn > 3, the modelled mass flow is larger but then approaches the experimental data again. For argon, the same behavior is observed, with an additional offset. A possible reason for this deviation pattern is the pressure regimes that are covered by different pressure sensors. Each pressure sensor exhibits a linear increase or decrease in deviation, so the systematic error of the model is likely due to measurement uncertainty, which is naturally largest at the outer region of each sensor measurement domain.

Diameter analysis

An interesting observation on the order of the size of molecular diameters can be made from figure 3.5. Apart from the van der Waals diameter consistently being the largest for each gas, the diameters show no order. The

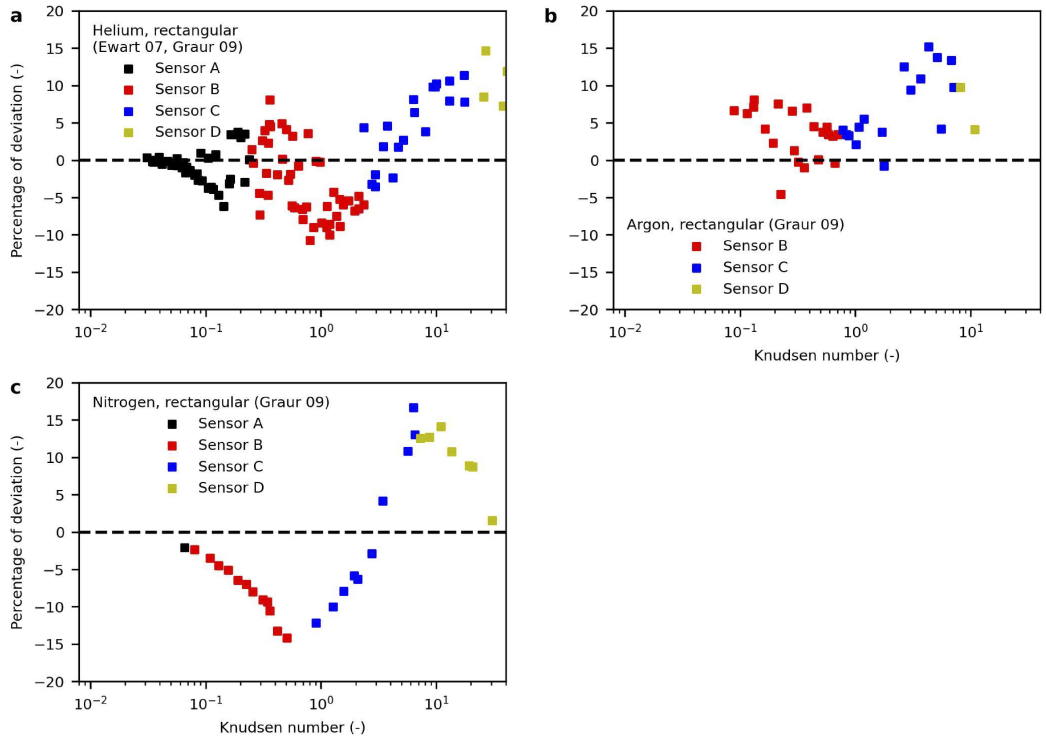

Figure 3.9: Deviation of modelled mass flow from experimental data for rectangular channels for **(a)** helium [74, 34], **(b)** argon [34] and **(c)** nitrogen [34]. The deviation shows some pattern that is strongly correlated to the pressure sensors used in different Kn regions.

kinetic diameter is larger than the diameter calculated from viscosity for helium but smaller for nitrogen, argon and carbon dioxide. The transition diameter, however, is smaller than the diameter calculated from viscosity for helium, argon and carbon dioxide but only smaller than the kinetic diameter for helium and argon. The transition diameter is almost equal to the kinetic diameter and the diameter calculated from viscosity for nitrogen and larger than the kinetic diameter for carbon dioxide. The smallest deviation from the transition diameter shows the viscous diameter for helium, nitrogen and carbon dioxide and the kinetic diameter for argon. Bondi states that the van der Waals diameter changes less for heavy atoms [56], which could explain why argon shows the smallest range of diameters. There are different trends when comparing the same diameter across gases. The van der Waals diameters and the diameters calculated from viscosity increase from helium via argon and nitrogen up to carbon dioxide. The same applies to the transition diameter. The kinetic diameter, however, follows this trend up to nitrogen but is smaller for carbon dioxide than for nitrogen and argon. This can be explained

by the measurement principle for kinetic diameters, which are obtained by molecular sieving experiments. Carbon dioxide can align lengthwise to pass very small pores, but this size is not representative of diffusion because it does not account for the longitudinal extent of the molecule. These inconsistencies can be attributed to different molecules behaving very differently in certain situations. On the one hand, the shape of molecules, which may be nonspherical, can contribute to this. On the other hand, because of their non-rigid nature, the diameter can be interpreted as an apparent size that changes with environmental conditions and is not exclusively geometrical. These environmental conditions are dominated by intermolecular interactions for the viscous regime, which become less significant for higher Knudsen numbers, and by molecular-surface interactions for measurements of the kinetic diameter, which are less considerable for smaller Knudsen numbers. In the transitional regime of approximately Kn = 1, both of these effects in sum are minimal. The transition diameter is, as all the other singular diameters, an effective diameter describing the flow and diffusion behavior and is therefore capable of describing non-spherical molecules as well.

3.3.6 Discussion

An intuitive way for rethinking rarefaction effects

Phenomena like that of rarefied gases are often hard to grasp because they are not relevant to or do not align with our day-to-day perception of macroscopic events. Describing those effects in a mathematical way like the Boltzmann equation may be correct, but is also abstract and not easy to develop an intuition for. Numerical approximations and empirical parameters can add to the confusion.

Each of the present model's constituents are simple, easy to understand and valid within their tight limitations. The superposition approach hardly makes the model more complex since it only combines the single constituents, thus increasing the limits of validity without sacrificing simplicity.

Intuition helps human beings to understand and qualitatively predict a system's behavior without having to calculate an accurate solution. One example is the Knudsen minimum - why would the dimensionless mass flow rise after a minimum? The dimensionless mass flow, in simple terms, describes the mass flow normalized to Δp. Why would, for same pressure differences but for smaller absolute pressures, the actual mass flow rise again?

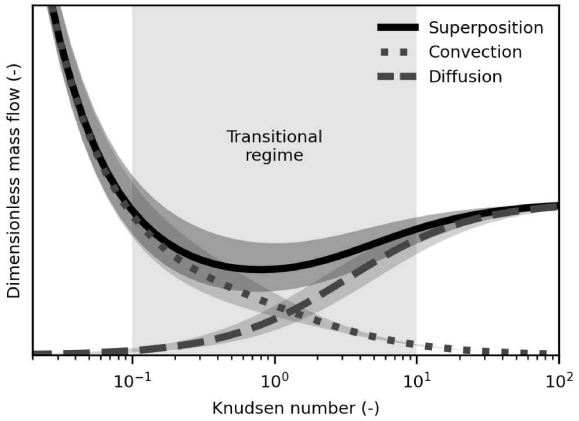

Figure 3.10: Schematic illustration of the individual transport terms of the superimposed model and their variation with the Knudsen number. The convective part decreases with rising Knudsen number while the diffusive part becomes dominant at Knudsen numbers larger than unity, because of the increasing mean free path. The diffusive part converges to a constant value at high Knudsen numbers where the surrounding geometry is the limiting factor for diffusion. The sum of both components reproduces the typical and well- known Knudsen minimum at approximately Kn = 1. The influence of the molecular diameter on the predicted mass flow is illustrated by the shaded areas.

The presented model explains this with the impact of each model's constituent. For small Knudsen numbers, the viscous part is the most significant, so the dimensionless mass flow decreases as expected. While corrected by a slip boundary condition, the viscous flow starts to vanish because of the limitation of the slip influence by the effective mean free path. The diffusive parts become more and more important for higher rarefactions. At the crossover of the mass flows of convective and diffusive flow, the minimum of the total mass flow emerges, see figure 3.10. After that, the diffusive mass flow rises even higher because the molecules are more and more free to move with lower pressure, thus increasing the diffusion coefficient, until the limiting free molecular flow is reached. This rise of diffusive flow leads to the increase of total mass flow after the Knudsen minimum.

Another aspect well demonstrated by the model is that it is unlikely that at different Knudsen ranges different effects come into play, with somehow arbitrary hard borders between those regimes. All parts of the model, each describing one effect (viscous flow, self-diffusion, free molecular flow) are *always* present, albeit to a different extent. There is no clear cut between e.g. the slip flow and the transition regime. It just happens so that the diffusive

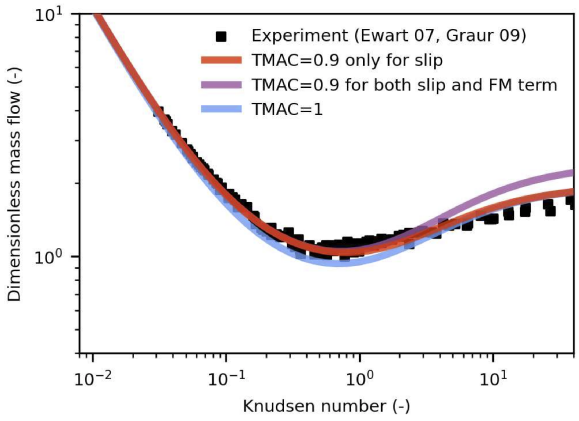

Figure 3.11: Dimensionless mass flow of helium in a rectangular channel [74, 34], calculated with the transition diameter but different TMACs for the slip convection term and the free molecular term.

flow becomes more important than the convective flow for Knudsen numbers around 1. The same goes for the transition and free molecular regime - by inversely adding the self-diffusive and free molecular flow, both parts are always present, but the self-diffusive part just becomes more and more negligible until asymptotically reaching free molecular flow.

Adapting TMAC vs molecular diameter

Instead of adjusting the TMAC, like it is usually done in the literature for slip flow models, the molecular diameter is adjusted in this work. To see why this is justifiable, not only the slip regime, but particularly the free molecular flow should be observed. As discussed above, the free molecular flow is not influenced by the molecular diameter. It would result in an overprediction of the free molecular flow if the TMAC was actually any smaller than 1. In figure 3.11 it is shown what would happen for different TMAC configurations of the model for rectangular channels. Since the transition diameter is already determined using circular channels, it is fixed for all cases. When setting the TMAC to 0.9 everywhere, an overprediction in the free molecular regime occurs. When setting the TMAC to 1 everywhere, the free molecular regime is described correctly, but the slip regime (and transition regime, where the slip also has an influence) is underpredicted.

Therefore, the slip expression needs to be larger than what it produces for a TMAC of 1. This can be achieved by setting the TMAC to 0.9 just for the slip expression. Again, it must be noted that this is not supposed to be

an actual description of the surface reflection behavior - it would be unreasonable to have diffuse reflection in the free molecular regime but somehow partly specular reflection for smaller Knudsen numbers, since the only influence on this behavior is the gas-surface interaction which is the same for a given gas-surface combination.

The only possible explanation left for this is an imperfect slip flow expression for rectangular channels, possibly arising from the complex geometry compared to a circular channel.

Scale invariance

The problem arising with surface diffusion, as discussed in section 3.2.1, is well-handled by this model. When keeping the width-to-height ratio constant, the G-Kn graph looks exactly the same for different channel sizes.

Limits

The model, like any closed-form analytical model, has a couple of assumptions. The flow needs to be laminar, the Reynolds and Mach numbers need to be sufficiently small. The flow needs to be an isothermal pressure driven flow, and the channels need to be straight, with a constant cross-section. Also, to be fully predictive, the transition diameter needs to be known. For this, rarefied gas flow measurements are needed. If not at hand, a good approximation may be using the diameter calculated from viscosity.

Fitting to less data and to rectangular channels

Theoretically, it would be sufficient to have data points just at Kn = 1 for determining the molecular diameter. However, it is important to be sure that the TMAC is set correctly, which can be validated by measurements in the free molecular regime. Additionally, the more data points are available, the smaller the uncertainty becomes. For example, the data for helium in circular channels consist of 32 data points. If the transition diameter calculation is performed only using 4 data points around Kn = 1, the result is $d_{trans} = 210 \pm 12$ pm - not much different to the 209 pm using all data points, but with a significantly higher uncertainty due to less data. The results for all four gases are shown in table 3.3. The only deviation exceeding the uncertainty is the one for nitrogen. This is because the truncated data only consists of data from Perrier et al. [37] and that data is quite different to the data by Varoutis

Table 3.3: Transition diameters in pm using different data. The truncated data for circular channels only uses 4 data points near Kn = 1.

Gas	Circular	Truncated circular	Rectangular
Helium	209 ± 3	210 ± 12	208 ± 2
Nitrogen	369 ± 9	333 ± 10	362 ± 14
Argon	317 ± 3	312 ± 6	333 ± 6
Carbon dioxide	419 ± 8	423 ± 8	—

et al. [72], see figure 3.8c. Because only one of the two datasets is used in the truncated version, this leads to a very different result.

Another approach would be to use data from rectangular channels instead of circular channels to determine the transition diameter in the first place. The results for this are also shown in table 3.3. For helium and nitrogen, the diameter are very similar to the ones using data from circular channels. For argon however, there is quite a deviation exceeding the uncertainty. A possible explanation is the amount of data for circular channels which is little comprehensive and does not cover the whole transition regime, the highest Knudsen number being 0.8. The data for the rectangular channels in turn covers a much larger Knudsen range while resulting in a slightly larger uncertainty. Which of those values is correct is hard to determine without further information like the general reliability of the experimental data.

3.3.7 Extension to arbitrary cross-sections

The model described above has explicit formulations for circular and rectangular cross-sections. It is, however, generally possible to extend the model to arbitrary cross-sections. For this, the implications for the model constituents are discussed.

Numerically solving the Smoluchowski equation

For circular and rectangular cross-sections, it is possible to use an analytical expression for the free molecular part, see section 3.1.4. When solving the Smoluchowski expression numerically, it is possible to apply it to arbitrary cross-sections. The procedure is implemented in Python using the `shapely` package for geometric calculations.

For the subdivision of the cross-sectional area, a rectangular boundary mesh is created using the maximum and minimum x and y coordinates of

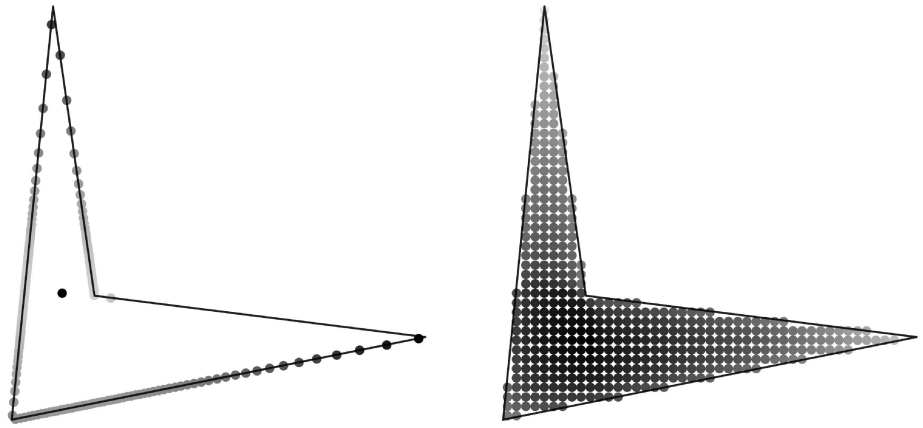

(a) (b)

Figure 3.12: An exemplary solution of the Smoluchowski equation for a sample cross-section. **(a)**: The sampling of equiangular boundary points for one specific area point. The color of the boundary points corresponds to the distance to the area point and therefore to their influence on the mass flow rate. The darker, the larger is the influence. **(b)**: The influence on the mass flow rate of each area point. It is clearly visible that the center points contribute more than the points near the boundary.

the given cross-sectional shape. This mesh is evenly subdivided. Then, a list of all points laying within the cross-sectional area are added to an `area_list`.

For each point in `area_list`, equiangular lines are created and their intersection with the boundary is determined. These intersections are added to `bound_list`. Such a list is created for each `area_list` point.

For each point in `bound_list`, the distance from its corresponding area point is calculated, see figure 3.12a. These distances are averaged and multiplied by 2π. After calculating this for each area point, see figure 3.12b, all the results are summed up and multiplied with the surface area of an area element, which is the same for all area elements due to the even subdivision. This result corresponds to the Λ in equation 3.16.

Numerical calculation of the effective mean free path

The model heavily relies on the knowledge of the effective mean free path which is part of the slip flow and self-diffusive term. This calculation could be performed analogously to the calculation of the Smoluchowski integral above. Each area point has a characteristic length which is the average of the distance to the boundary - see figure 3.12a. This characteristic length could be

combined with the classical mean free path via equation 3.28. This effective mean free path can be directly used to calculate the self-diffusive flow via equation 3.15.

The effective mean free path also influences the slip flow, see for example 3.8. With a knowledge of the effective mean free path, the actual viscous flow still needs to be determined, e.g. by numerically solving the Navier-Stokes equations. This is still much more efficient that numerical methods related to the Boltzmann equation which are much more expensive in terms of computational power than the Navier-Stokes equations.

Chapter 4

Rarefied gas flow in surface functionalized channels[1]

To investigate the effect of surface functionalization on the mass flow of rarefied gases and to exclude the irregularity of porous media, mass flow rate experiments in straight, rectangular channels with and without functionalization are performed. The results are analyzed using a novel methodology and are compared to the previously introduced analytical model.

The preparations of the experiments, like channel manufacturing, characterization and functionalization, are executed at the University of Bremen. The mass flow experiments are conducted at two places for two different channel geometries: at the Karlsruhe Institute of Technology, KIT, using the TRANSFLOW facility for the large channels; and at the IUSTI laboratory in Marseille for the small channels.

4.1 Mass flow rate measurements in literature

The most thoroughly studied rarefied gas flow is the one in the slip regime, which is also the easiest to describe with analytical models [83]. Experimental data for slip flow in circular [63, 84, 85] and rectangular channels [86, 35, 87, 32] is found in abundance. Mass flow measurements extending into the transition regime where conducted for circular tubes by [88, 89] and for rectangular channels by [90]. Data for circular tubes from the slip regime up to the free molecular regime is given by [18, 91, 92, 93, 37, 94], for circular, square, triangular and trapezoidal channels by [72], and for high-aspect rectangular channels by [95, 96, 97, 74, 34].

[1] Parts of this chapter have been published verbatim in [82].

While measurements in microchannels are done with plain surfaces, functionalization is well-known in the membrane community to increase selectivity [3]. An important result of measurements using irregular porous media with functionalized surfaces is that applying such surface functionalization significantly reduces the gas flow [52, 48, 49]. However, in [31] it was shown that the length of the functionalization molecule is the determining factor which impact the flow reduction. The chemical composition of the functional group itself does not influence the gas flow.

4.2 Channel preparations

4.2.1 Manufacturing

To get geometrically well-defined channels, they are etched into silicon wafers. For surfaces as smooth and regular as possible, wet etching [98, p. 237ff] is chosen over DRIE etching [98, p. 255ff], even though this leads to trapezoidal channel cross-sections. Because of the large width to height ratio of around 30, an effect of non-perpendicular side walls is negligible. The wafers are etched from both sides to create a stack with half of the channels on one side and half of the channels on the other side.

The channels are aligned on the wafer as shown in figure A.1 and figure A.2. After etching the channels, their dimensions are measured (see 4.2.2). The channels are then closed by anodic bonding of borosilicate glass which acts like a ceiling on a room. Finally, the wafer is cut at defined positions to get the needed channel length.

Two different channel geometries are used, see table 4.1. For the mass flow measurements at the IUSTI laboratory, a stack of 100 parallel small channels is manufactured because of preceding experiments with different requirements. However, to perform single-channel measurements, 99 channels are closed by using epoxy glue (UHU Plus Endfest). For the KIT laboratory, a stack of 20 large channels in parallel is used for increasing the mass flow

Table 4.1: Channel characteristics.

Channel	Laboratory	Height h [µm]	Width w [µm]	Length L [mm]	Parallel channels
small	IUSTI	5.21 ± 0.1	145.22 ± 0.21	12.07 ± 0.06	1
large	KIT	48.2 ± 0.3	1469 ± 6	12.56 ± 0.06	20

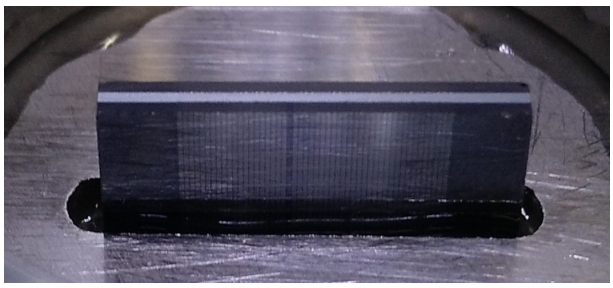

Figure 4.1: A stack of channels glued into a metal socket. A single channel is filled with water, visible as a darker vertical line near the center of the stack.

to meet the facility's requirements. To confirm that closing 99 channels was successful, water droplets are put on the channel stack under a microscope using a mirror configuration shown in figure 4.5a. Here, it could clearly be seen that the water only enters the single open channel because of capillary forces. This is also visible without a microscope, see figure 4.1.

For integrating the microchannels into the measurement setups, they are glued with the same epoxy into a socket with KF (ISO quick release) flanges on each side for the experiments at the IUSTI, see figure 4.2a, and into a CF (ConFlat, cooper-sealed) flange for the experiments at the KIT, see figure 4.2b. The TRANSFLOW facility can be connected to by using a CF250 flange. Because the microchannels are much smaller than this and because each stack of channel will need its own flange, CF63 flanges are used as a socket for the channel stacks. The CF63 flanges are attached to the CF250 flange by a custom-made adapter by Vacom.

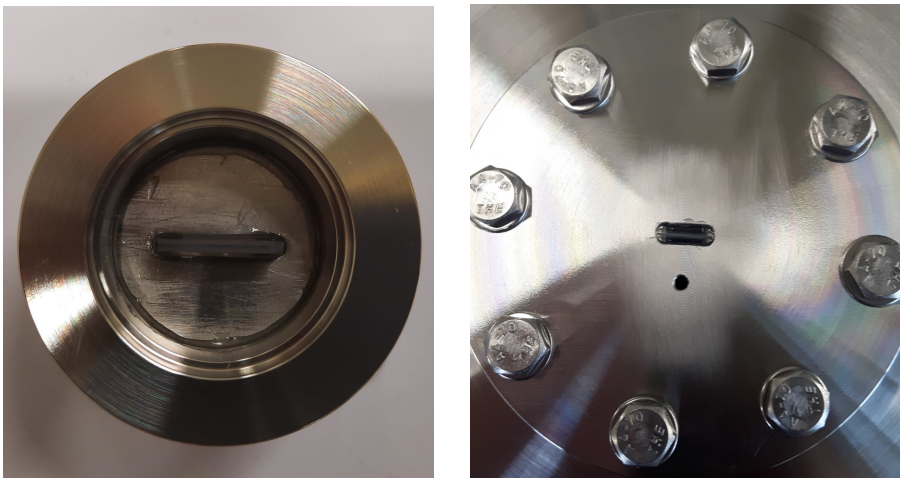

(a) (b)

Figure 4.2: Channel sockets for **(a)** the IUSTI experimental facility and **(b)** the TRANSFLOW experimental facility.

4.2.2 Characterization

The microchannels are first characterized using vertical scanning interferometry, an optical, non-destructive method for measuring the surface profile using white light and special mirau lenses [99, 100]. The vertical resolution of VSI is typically about 1 nm while the lateral resolution depends on the used lens. For the large channels, multiple pictures covering all 10 channels per side of a stack are stitched together by the software. For the small channels, this was not feasible and single pictures of each channel are analyzed.

The analysis is performed by a self-developed script. As a first step, the height profile across one channel (for the small channels, see 4.3a) or across all channels (for the stitched images of the large channels, see 4.3b) along a line is extracted. The slope of this height profile is then analyzed with the Python package `peakutils` to extract peaks. The peak positions are used to determine each channel width and height. This is repeated for height profiles along different lines across the height map to avoid uncertainty due to local noise.

This procedure is executed at different positions on the wafer to account for manufacturing irregularities across the wafer. Finally, by taking all calculated channel widths and heights, the mean and standard deviation of widths and heights is calculated.

The lengths of the channels is set by cutting the wafer at defined positions. After cutting, the length is measured using a caliper gauge. The channel dimensions are given in table 4.1.

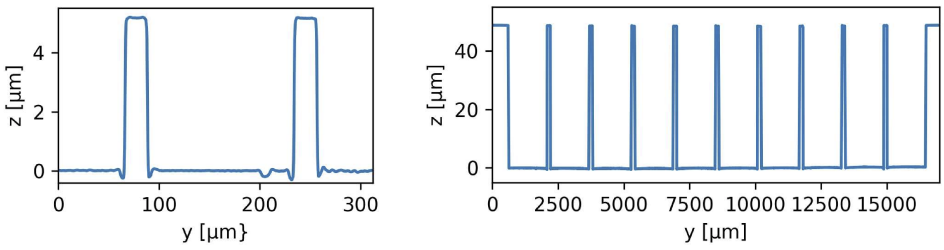

(a) (b)

Figure 4.3: Height profiles from VSI measurement. **(a)**: A single profile of a small channel. **(b)**: Profile of a stitched measurement of large channels.

4.2.3 Functionalization

As described in section 4.1, the largest influence of any surface functionalization is expected from large molecules. Therefore, hexadecyltrimethoxysilane (HDTMS) is used to alter the interaction between gas and wall. Since the largest effect is expected in the small channels, only those are functionalized. The molecules are attached to the channel walls by chemical vapor deposition (CVD) [101, 102]. To perform CVD, an experimental setup was built, see figure 4.4. The main components are the three-neck round-bottom flask, in which the liquid silane is placed, and the socket to keep the channel in place and seal it against the atmosphere.

The system is evacuated and flushed with nitrogen. After that, HDTMS is injected into the three-neck round-bottom flask with nitrogen excess pressure. While heating the flask in an oil bath to 150 °C, the flask is evacuated until condensate on the flask is visible. Then, vacuum is only pulled from the other side of the channel, creating a pressure difference along the channel and forcing the silane through it where it reacts with the surface [103, p. 539]. This process runs for 62 hours. The system is then flooded with air, and the channels are extracted.

To evaluate the result of functionalization, the contact angle of water and air inside the channel is measured. For this, the microchannels are observed through a mirror construction, see figure 4.5a, with an incident light microscope while water is inserted into the channel using a pipette. The results ($16 \pm 1.3°$ for plain, $36.3 \pm 2.2°$ for functionalized) show a clear difference

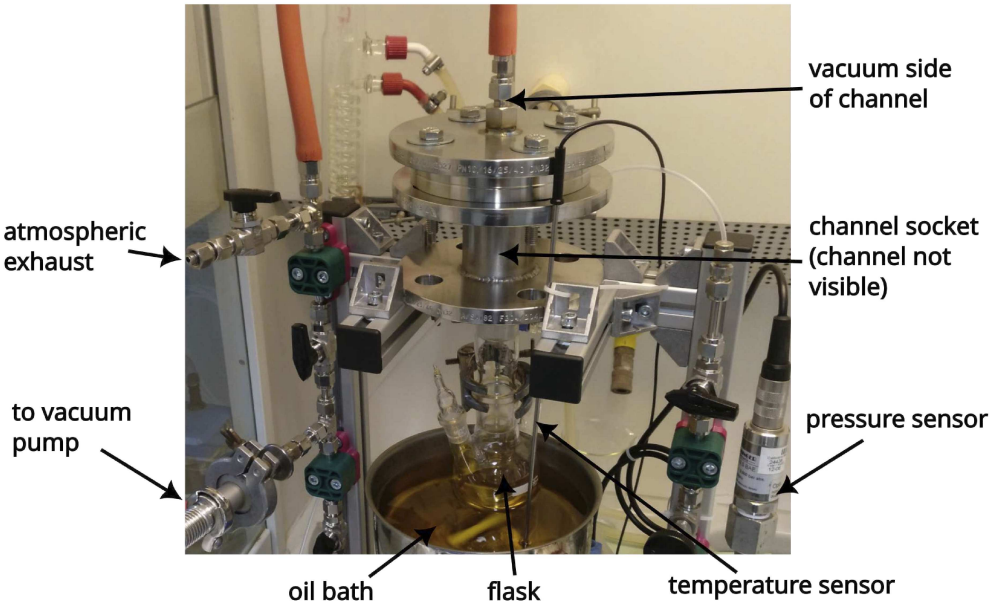

Figure 4.4: The functionalization setup.

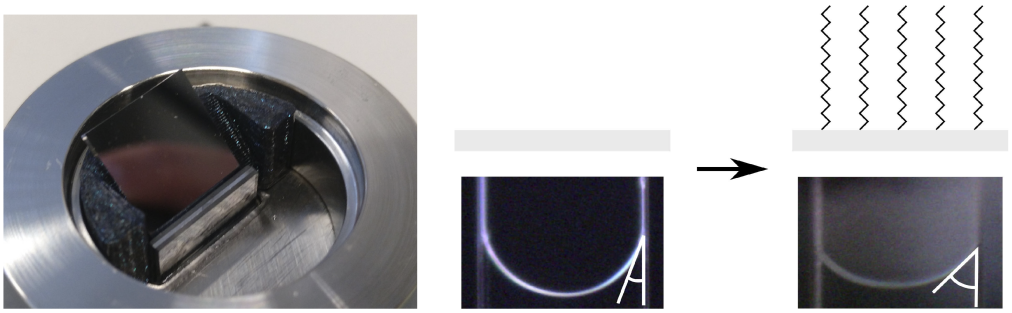

(a) (b)

Figure 4.5: **(a)**: The microscope setup to optically access the small channels using a mirror. **(b)**: Evaluation of functionalization by contact angle measurement with water. Left: the plain channel. Right: the channel with HDTMS functionalization.

and therefore a successful functionalization, see figure 4.5b. The analysis of the contact angle is performed with ImageJ [104] using the `Contact Angle` plugin.

4.3 Mass flow measurement facilities

In both facilities, the constant volume method is used. This means that pressure changes in the upstream (and optionally downstream) reservoir are constantly measured, while the mass flow rate is deduced from the slope of the pressure evolution over time. The setups are schematically depicted in figure 4.6.

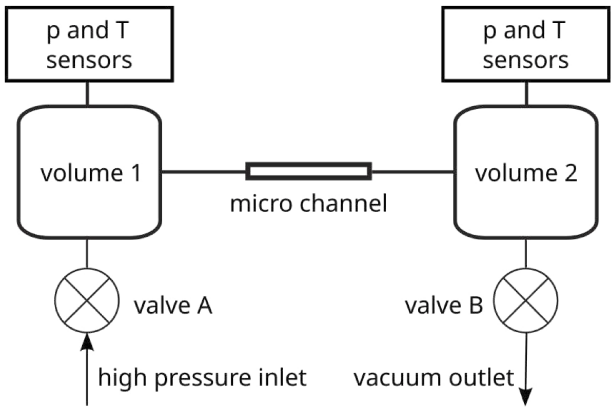

Figure 4.6: Schematic view of the experimental setups. During an experiment, valve B is closed for the IUSTI setup and open for the TRANSFLOW setup. Valve A is closed in both setups.

4.3.1 TRANSFLOW

For the large channels, the TRANSFLOW facility at KIT is utilized, see figure 4.7a. Details about the facility can be found in [105]. The volume of the upstream reservoir including adapter flange is $V_1 = 0.606 \pm 0.012\ m^3$. In the downstream reservoir, two turbomolecular pumps keep up a vacuum. The volume of the downstream reservoir is $V_2 = 1.2m^3$. The whole facility can be heated and kept isothermal within 1 degree.

The TRANSFLOW facility originally uses a constant mass flow technique. By applying a constant mass flow to the upstream volume, steady state is reached after a while when the gas flow through the channels is as large as the applied mass flow and the equilibrium pressures can be measured. The time to reach this equilibrium depends on several factors, like the mass flow and the channel size. Another factor which can't be changed for the given facility is the upstream volume. The larger this volume is, the longer it takes to reach equilibrium. Because the TRANSFLOW facility was designed to work with macro channels [105], the upstream volume is correspondingly large. Because the channels are so small, the needed pressure difference for a given mass flow needs to be large compared to larger channels, which means that the upstream pressure needs to be quite high. To get to such a high pressure, it takes a long time using a constant mass flow in agreement to the relatively low mass flow through a microchannel. As an example, let's consider an experimental run at Knudsen = 0.7 for the large channel with helium. The corresponding inlet pressure is about 1300 Pa, and mass flow through the channels is about 6e-10 $\mathrm{kg\,s^{-1}}$. At 1300 Pa and 20 °C, there are 1.3e-3 kg of helium in the upstream vessel. Setting the MFC to the predicted mass flow rate through the channels, it would take at least 25 days to reach this pressure, and that is without any flow through the channel, which would reduce the pressure rise more and more, therefore significantly increasing the needed time.

Because these time scales are unfeasible, a heuristic approach to reduce the time until equilibrium is used: using analytical models, the approximate pressure needed for a given mass flow is calculated. High mass flow is then used to get to that pressure. When the pressure is reached, the actual mass flow is applied. Using this approach, the pressure just needs to adapt a little until equilibrium is reached. However, even using this enhancement, the time scales are way too long for the many data points needed.

As an alternative, the constant volume method is used. By starting with a given inlet pressure (reached by using high mass flows to introduce the

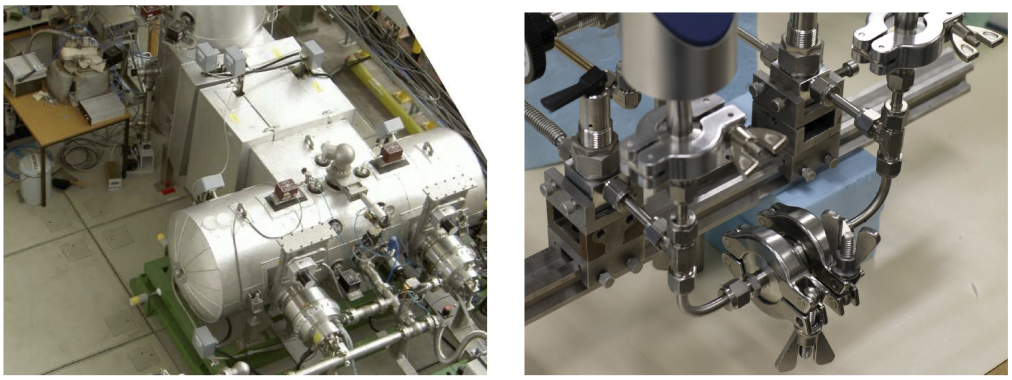

(a) (b)

Figure 4.7: **(a)**: Experimental facility TRANSFLOW at the KIT laboratory. The cylindrical structure at the bottom is the downstream volume with the turbomolecular pumps attached. The cubic structure near the center is the cover of the channel. At the top of the picture, part of the upstream volume is visible. Photograph used with permission of Stylianos Varoutis. **(b)**: Experimental facility at the IUSTI laboratory. At the top of the image, the pressure sensors attached to the system via KF flanges are visible. At the bottom, between the two KF flanges, is the microchannel. Left is the upstream volume, right is the downstream volume.

needed amount of gas), the mass flow controllers are switched off. Gas flows from the upstream through the channels to the downstream volume, thus reducing the upstream pressure. This pressure decreases over time is measured and transformed to a mass flow using the known upstream volume.

To measure the upstream and downstream pressures, capacitance diaphragm gauges by MKS are used with maximum measurement range of 133 300 Pa, 1333 Pa and 133.3 Pa at the dosing dome or 13.33 Pa at the pumping dome, respectively. Additionally, each reservoir has a hot cathode gauge by Granville-Philips for very low pressures.

4.3.2 IUSTI laboratory

The facility at the IUSTI laboratory was rebuilt from scratch to provide the appropriate conditions for the experiments. The setup uses the constant volume method based on pressure measurements in both upstream and downstream volumes to determine the mass flow rate through a microchannel fixed between the two volumes, see figure 4.7b. To minimize the experimental time needed for a data point, the constant volumes 1 and 2, see figure 4.6, are reduced, and they consist merely of the piping. Most of the piping was done using Swagelok fittings. The channel socket consists of two KF25

flanges with a pipe piece. In this pipe piece, the microchannels are attached. The KF flanges are then connected to their counterparts in the experimental setup to allow for an easy change of channels without disassembling the facility.

The pressure sensors are connected to the facility with KF16 flanges. There is only one sensor connected to each volume to minimize the volume. Therefore, depending on the experimental conditions, the sensors need to be swapped to stay within the measurement range of the sensor.

During each experimental run the room temperature is measured by K type thermocouples in combination with four-wire Pt100 for cold junction compensation. The temperature is stable within 3.1 K during an experimental run with a maximum length of around 17 hours and corresponds to room temperature.

With this setup it is possible to measure pressures in the range of 10 to 100 000 Pa with capacitance diaphragm gauges having an uncertainty of 0.2 %. Two gases are used, helium and carbon dioxide, provided by Air Liquide (France) with a purity of 99.999 %. The available pressure range corresponds to a Knudsen number range of 0.03 to 10 for helium and of 0.01 to 3 for carbon dioxide. A detailed description of a similar setup using the same measurement components is given in [106].

4.3.3 Facility volumes

To determine the volumes of the facility, two techniques are applied.

For the IUSTI facility, pressure equilibration is used in combination with a known volume V_2 to calculate an unknown volume V_1. Both volumes have different initial pressures p_1 and p_2. The volumes are connected by a valve, which is opened and the equilibrium pressure p_{eq} is measured. V_1 can then be calculated by

$$V_1 = -\frac{\Delta p_2}{\Delta p_1} V_2 \tag{4.1}$$

where $\Delta p_i = p_{eq} - p_i$ is the difference between initial pressure and equilibrated pressure in volumes 1 and 2, respectively.

The IUSTI facility consists of 4 volumes: the known volume, an intermediate volume and the upstream and downstream volumes which are to be determined. First, the intermediate volume was calculated by filling up the known volume with gas up to a known pressure p_2. That volume is then closed with a valve, and the rest of the facility is evacuated to p_1. The upstream and downstream volumes are closed. Then, the known volume is

opened again to equilibrate the pressure of the known volume and the intermediate volume to p_{eq}. With this information the intermediate volume is determined. Using the same technique, this time using the sum of the originally known volume and the intermediate volume as the new known volume, the upstream and downstream volumes are determined one by one. Each volume including the intermediate one is determined 3 times for uncertainty calculation. Using error propagation, this results in an upstream volume of 17.57 ± 0.37 cm^3 and a downstream volume of 17.2 ± 0.58 cm^3.

For the TRANSFLOW facility, a calibrated mass flow controller is used to inject a constant mass flow rate into the upstream volume while monitoring the pressure rise. The slope of the pressure can then be used to calculate the volume when the mass flow is known. The uncertainty of the volume is due to the uncertainty of the mass flow controller provided by the calibration certificate. This results in an upstream volume of 0.606 ± 0.012 m^3.

4.4 Method for optimized mass flow rate measurement

Because measurements of the mass flow rate of rarefied gases in microchannels are inherently noisy and unstable due to the very small mass flow and accordingly small pressure chances, a method for making optimal use of the acquired data is developed. For the preceding conversion from measured Volts to Pascals, see A.3.

4.4.1 General mass flow rate calculation

When the pressure in the volumes is changing due to the mass flow through the channel and it does so slowly in relation to the time needed to reach an equilibrium, the system is in a quasi-stationary state and the change of the system can be considered as a succession of local equilibria.

Because the temperature during an experiment is kept stable, the mass flow rate $\dot{m}$ is simply

$$\dot{m}_i(t) = \frac{V_i}{RT/M}\dot{p}_i(t). \tag{4.2}$$

If both valves A and B (see figure 4.6) are closed, which is the case for the IUSTI facility but not for TRANSFLOW, the mass conservation between volume 1 and 2 results in

$$\dot{m}_1(t) = -\dot{m}_2(t) \tag{4.3}$$

using the convention of a negative mass flow for a reduction of mass inside a volume.

To calculate the mass flow rate the pressure variation in a tank over the time is measured. At the IUSTI laboratory, the pressure in both upstream and downstream volumes changes: the higher upstream pressure decreases over time while the lower downstream pressure increases, until an equilibrium pressure, p_{eq}, is reached in both tanks. At the KIT laboratory, the downstream volume is continuously evacuated, therefore only the upstream pressure change is used for mass flow rate calculation.

These pressure variations in time can be fitted using either a linear function or more generally using an exponential function. To be able to cover a larger experimental range where the mass flow might not be constant, an exponential function is chosen here, as proposed in [107, 108]:

$$p_i(t) = p_{eq} + (p_i^* - p_{eq})e^{-t/\tau_i}, \tag{4.4}$$

where p_{eq} is the equilibrium pressure for $t \to \infty$, p_i^* is the initial pressure, and τ_i is the pressure relaxation time, which characterizes the speed of pressure rise or drop. The measured pressure variation in time is fitted using equation (4.4) with τ_i and p_i^* as the fitting parameters. p_{eq} is approximated using the initial pressures and the tank volumes. The pressure derivation in time is calculated as

$$\dot{p}_i(t) = -\frac{p_i^* - p_{eq}}{\tau_i} e^{-t/\tau_i} \tag{4.5}$$

The mass flow rate is then calculated from

$$\dot{m}_i(t) = \frac{V_i}{RT/M} \frac{p_i^* - p_{eq}}{\tau_i} e^{-t/\tau_i} \tag{4.6}$$

which simplifies for $t = 0$ to

$$\dot{m}_i = \frac{V_i}{RT/M} \frac{p_i^* - p_{eq}}{\tau_i} \tag{4.7}$$

to get the mass flow rate at the beginning of the experiment. The Knudsen number associated to this mass flow is calculated using $p_m^* = 0.5\,(p_1^* + p_2^*)$.

The measured mass flow rate is corrected with a previously measured leakage or outgassing mass flow rate by addition or subtraction when the leakage or outgassing is significant. The leakage mass flow rate is determined by setting the pressure equally low in both volumes and by monitoring the pressure rise over time. The magnitude of the influence of the leakage

correction varies strongly and is quantified in A.4.

Because the mass flow is calculated using the pressure drop in the volumes, the experiments need to run for a certain time to have a significant change in pressure compared to the sensor noise. However, too long measurement times introduce external influences like temperature fluctuation which can impact the assumption of isothermal conditions required for equation 4.2. Too short measurements in turn can lead to a high uncertainty due to the small amount of data available for a fit.

To find the ideal amount of data, the measurement uncertainty is minimized. The measurement uncertainty consists of two parts: one part describing the reliability of the chosen amount of measurement data using *data fragments*, and the other part describing the physical uncertainties of pressure sensors, temperature fluctuations and channel and facility geometries.

4.4.2 Variability of data fragments

The *variability of data fragments* methodology differs for the IUSTI and the TRANSFLOW facilities. In case of the IUSTI facility, an important criterion for a successful run is the match of inlet and outlet mass flows, see equation (4.3), which are independently calculated using the respective pressure drops. This criterion is not fulfilled if the signal-to-noise ratio is too low which would introduce randomness to the mass flows and make them likely differ. Also, temperature fluctuations would create a mismatch because a temperature rise decreases the calculated mass flow rate in volume 1 and increases the calculated mass flow rate in volume 2.

Accordingly, the issues above can be addressed by looking at the difference of the mass flow rates calculated in volumes 1 and 2. One single, long experimental run is used. Only parts of this run are analyzed to simulate different lengths of experimental runs. These parts are taken at different positions and are of different length, resulting in *time windows* as depicted in figure 4.8. This results in a two-dimensional array of fictive experiments, each having their analyzed mass flow rates and their mass flow difference between volume 1 and volume 2. An example of a two-dimensional array, visualizing the relative difference between volume 1 and volume 2 mass flow rates, is shown in figure 4.9a.

For the runs with small width, very low deviations are right next to very high deviations. This is the result of a low signal-to-noise ratio of little data. Simply choosing the data fragment having the smallest deviation

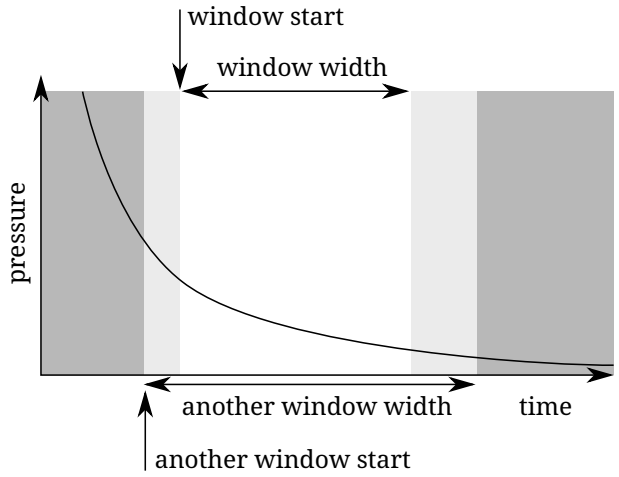

Figure 4.8: Depiction of two *time windows*. A *time window* is defined by a start and a width. One window consists of the data with white background. Another window consists of the data with white and light gray background: it has an earlier start and a larger width.

would therefore be a matter of chance and not a reliable choice.

To tackle this problem, a second criterion is imposed: not only does a single fragment need to have a low difference between inlet and outlet, but an *area* of fragments should stay below a certain deviation. This is done by applying a threshold to the array of mass flow differences and searching for an area large enough to host a circle with a radius of 20 % of the width of the time window at the circle's center. This corresponds to a possible shift of the window by 20 % of the window width and a scaling of the window by 20 % while staying within the threshold. To avoid noise problems, a minimum of 3 time windows should be covered by the radius. To include as much data as possible for the fit, longer runs are prioritized if ambiguity arises.

The threshold is increased until an area fulfilling the 20 % criterion is found. That process is depicted in figure 4.9b to 4.9d. The Knudsen number and the dimensionless mass flow rate, defined by equation (3.19), are taken from the run in the center of the circle.

In case of TRANSFLOW, there is no difference between mass flow rates of volumes 1 and 2 because only volume 1 is considered, so the methodology is slightly different. Each entry of the array of data fragments is investigated one by one. For each entry, the difference to all other fragments is calculated. This results in an array of mass flow differences - not between volumes 1 and 2, but between the current and all other data fragments, see figure 4.10a. To this difference a threshold is applied like above and a check for an area

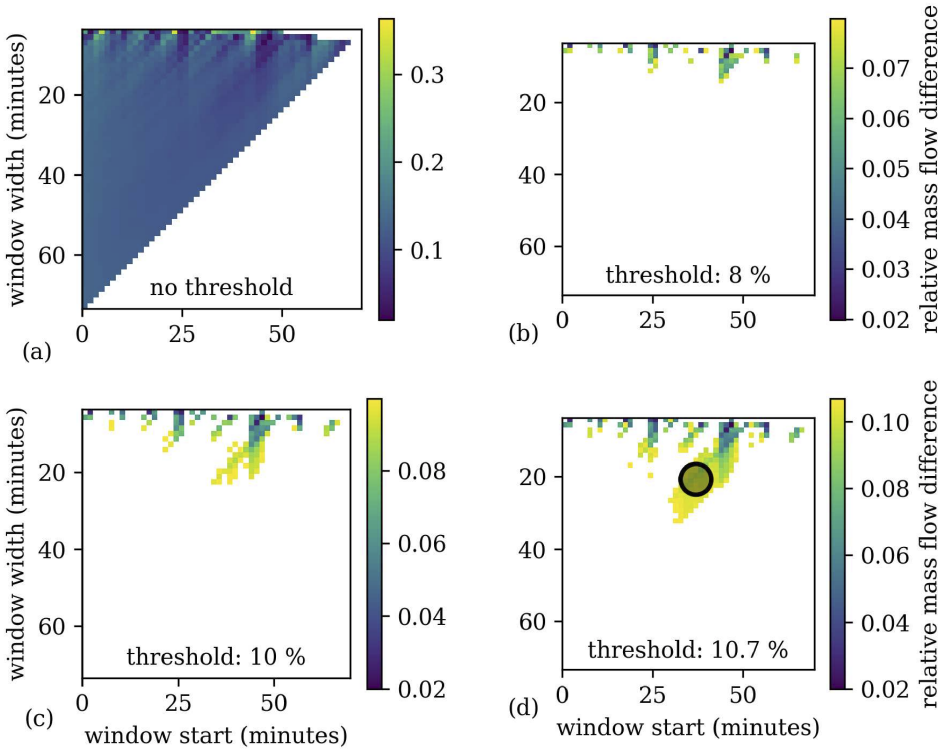

Figure 4.9: Differences between mass flow rates calculated from upstream and downstream pressure changes. Each square corresponds to a fragment of the data defined by its corresponding window start and window width. The lower right part is empty because the window would end outside the available data. This results in (50x50)/2 = 1250 single evaluations. Some samples at the top are empty because no fit for that data was found. **(a)** The full array without any threshold. **(b)** A threshold of 8 %; only very few fragments fulfill this threshold. No sufficiently large area can be found. **(c)** A threshold of 10 %. More fragments fulfill this threshold, but not enough to find a sufficiently large area. **(d)** A threshold of 10.7 % results in a structure where a sufficiently large area can be found (marked with a circle). Therefore, the corresponding relative uncertainty of mass flow rate due to the data fragment method is 5.35 %.

fulfilling the 20 % criterion is performed. If no area is found, the next entry of the array is investigated by re-calculating the difference to all other fragments, applying the threshold and checking for an area. If after cycling through all entries no area is found, the threshold is increased and all entries are investigated one by one again until an area is found.

This threshold is then used for an uncertainty which is defined via the population standard deviation [109, p. 111] as half of the relative difference between inlet and outlet mass flow rates or half of the relative difference

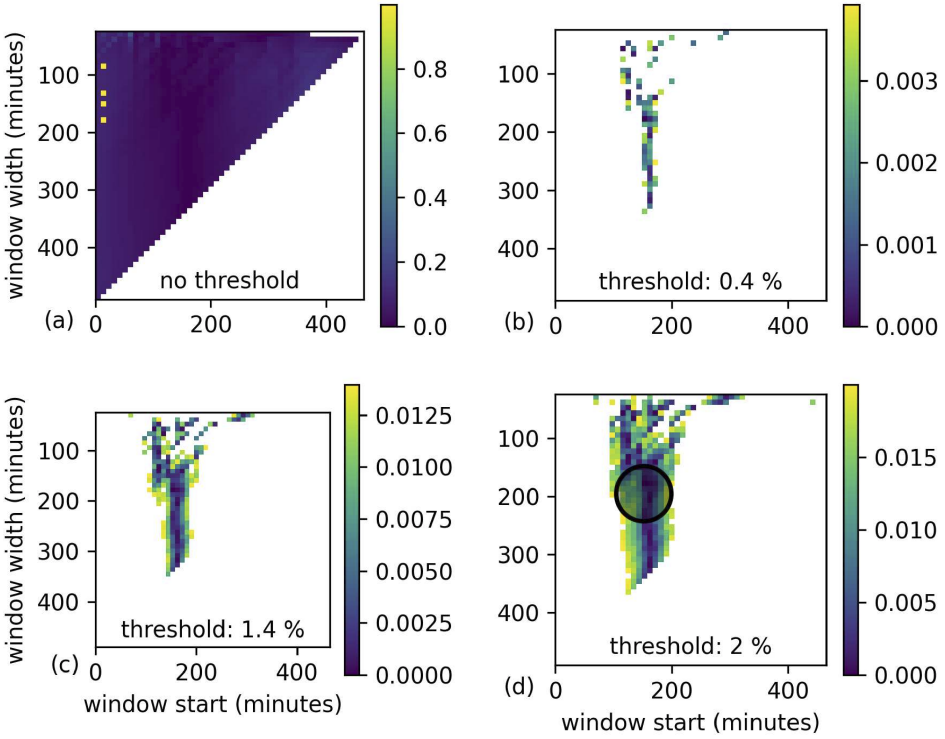

Figure 4.10: Differences between a mass flow rate of a single fragment and all other fragments. **(a)** The full array without any threshold. **(b)** A threshold of 0.4 %. **(c)** A threshold of 1.4 %. **(d)** A threshold of 2 % results in a structure where a sufficiently large area can be found (marked with a circle). Therefore, the corresponding relative uncertainty of mass flow rate due to the data fragment method is 1 %.

between the current fragment and all other fragments within the found area.

Generally, the method using two volumes should be preferred because the successful comparison of two separate mass flow balances is a strong indicator of correct measurements. Using only one volume leaves more room for systematic errors because influences like leakage or adsorption and desorption effects are not directly detectable.

4.4.3 Temperature fluctuations

During an experiment, the temperature is assumed to be constant, but still fluctuates due to room temperature changes and controller behavior. For the IUSTI facility, the room temperature is monitored during an experimental run. The TRANSFLOW facility directly measures the temperatures of the facility itself. The temperature uncertainty is calculated by taking the standard

deviation of all temperature data points during an experimental run. The largest fluctuation is 3.2 K.

4.4.4 Monte Carlo uncertainty sampling

To calculate the influence of the pressure sensor uncertainty on the uncertainty of the pressure drop, a Monte Carlo sampling [110] is performed using a self-developed implementation. The method works by creating many "virtual" experiments (*samples*) based on the actual measurement data and known uncertainty influences. These experiments are evaluated and the standard deviation between these samples is the uncertainty due to the known uncertainty influences.

A sample is created by taking the measured pressure over time and adding a value to each data point. This value is separately calculated for each data point. It is drawn from a distribution characterizing the uncertainty of the pressure sensor. The sensor uncertainty is assumed to follow a normal distribution. Therefore, for each data point a value is drawn from a normal distribution with a width of the sensor uncertainty at that pressure value.

The uncertainty is a constant factor of 0.2 % for the experiments at the IUSTI facility. For TRANSFLOW, the uncertainty is dependent on the pressure. Therefore, the calibration certificate is used for each data point to extract the correct uncertainty.

For each sample, a fit through the sample pressure data is calculated. An example of that procedure is shown in figure 4.11.

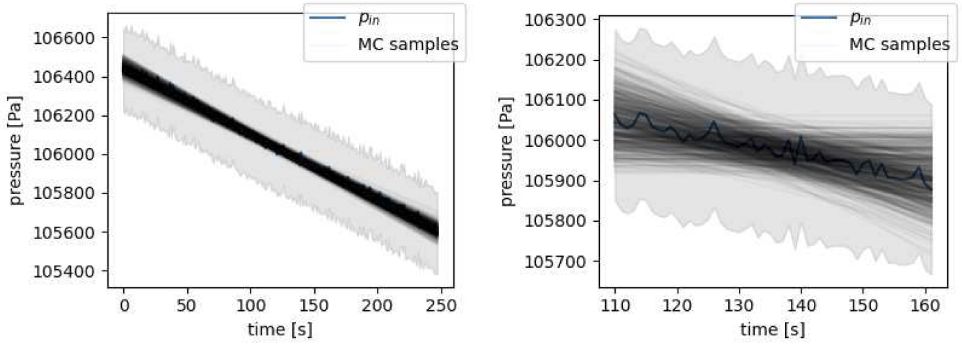

(a) (b)

Figure 4.11: Monte Carlo sampling. The gray background shows the measurement data ± the sensor uncertainty. The gray lines are the fits of the samples. **(a)**: Sampling for the whole data of one experimental run. **(b)**: Sampling for a smaller part of the data.

The pressure drop is calculated for each sample. This process is repeated with many samples until a convergence of the mean of the pressure drops resulting from the samples is reached. The standard deviation of the pressure drop between the samples is the uncertainty of the pressure drop due to the pressure sensor uncertainty. In figure 4.11a and 4.11b, it can be seen how the amount of data influences the deviation of the samples. In figure 4.11b, the different samples show very different slopes, while in figure 4.11b, they are quite similar.

4.4.5 Error propagation

The influence of the uncertainties of pressure drop (see section 4.4.4), temperature (see section 4.4.3), facility volumes (see Section 4.3.3) and channel geometry (see section 4.2.2) on the dimensional and dimensionless mass flow rates is determined using standard error propagation of independent variables. This is implemented using the Python package `uncertainties` [111].

4.4.6 Minimization of total uncertainties

The total uncertainty is the sum of the uncertainty coming from the data fragment analysis, see Section 4.4.2, and the uncertainty calculated by error propagation, see Section 4.4.5. To minimize the total uncertainty, the best data fragment needs to be determined for which an optimization of the uncertainty with the threshold as a free parameter could be performed. But, as seen in figure 4.12, while there is a clear trend of the total uncertainty decreasing until a point end then increasing again, the shape of the uncertainty over the threshold is very jagged, so a local optimization would get stuck in a local minimum. While global optimization is a possibility, it proved easier to just sample the thresholds logarithmically and perform the complete calculation of the total uncertainty for each threshold. Thresholds with no valid 20 % area are discarded. The threshold with the lowest total uncertainty is chosen, and the data fragment associated with this threshold is determined as the optimal data fragment. If this total uncertainty is still larger than 20 %, that experimental run is discarded. This is by no means a polishing of data, but rather as a tool to identify experimental runs which have issues at the execution level, like excessive adsorption and desorption effects or leakage.

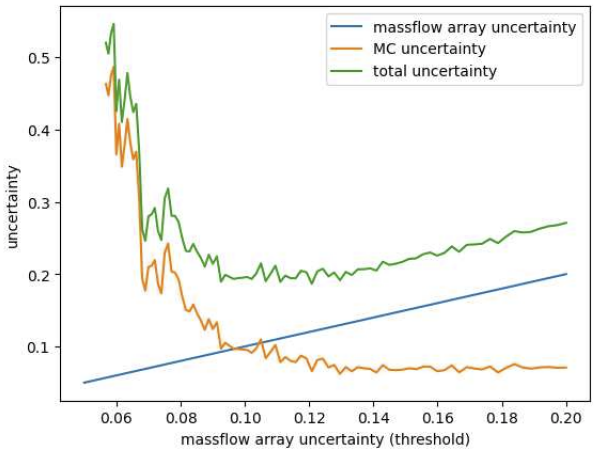

Figure 4.12: The sampling of thresholds with the two parts of the total uncertainty.

4.5 Experimental Results

The results of the experiments for both the plain and the HDTMS-functionalized channels with helium and carbon dioxide are shown in figure 4.13a together with the analytical curve. The so-called Knudsen minimum [18] at around Kn=1 is well visible. The dimensionless mass flow rate converges to a constant value for large Knudsen numbers as expected [68]. One experiment, although fulfilling the criterion of an uncertainty of < 20 %, is considered an outlier and is therefore plotted in gray color and excluded from the figures 4.13b-4.13d and further discussion.

It is clear from figure 4.13a that HDTMS has no significant influence on the gas flow. This finding is different to previous measurements carried out in much smaller geometries [31]. The absence of an impact of the functionalized surface may be explained by the fact that the influence of gas-surface interaction on the mass flow rate depends not only on the rarefaction level but also on the channel surface-to-volume ratio. This ratio for the channels used in experiments at the IUSTI laboratory is much smaller (0.4 μm^{-1}) than that of the experiments reported in [31] (300 μm^{-1}, with a pore diameter of 20 nm). Therefore, the highest surface-to-volume ratio for the channels used in the experiments presented here is likely still too small to have any influence on the mass flow rate.

When comparing the experiments with the analytical model introduced in section 3.3 (figure 4.13b) as well as with simulation data based on the linearized S-model kinetic equation from [112] (figure 4.13c) and that based on the linearized BGK kinetic equation [72] calculated for [82] (figure 4.13d), all three results look very similar with little deviation between the analytical

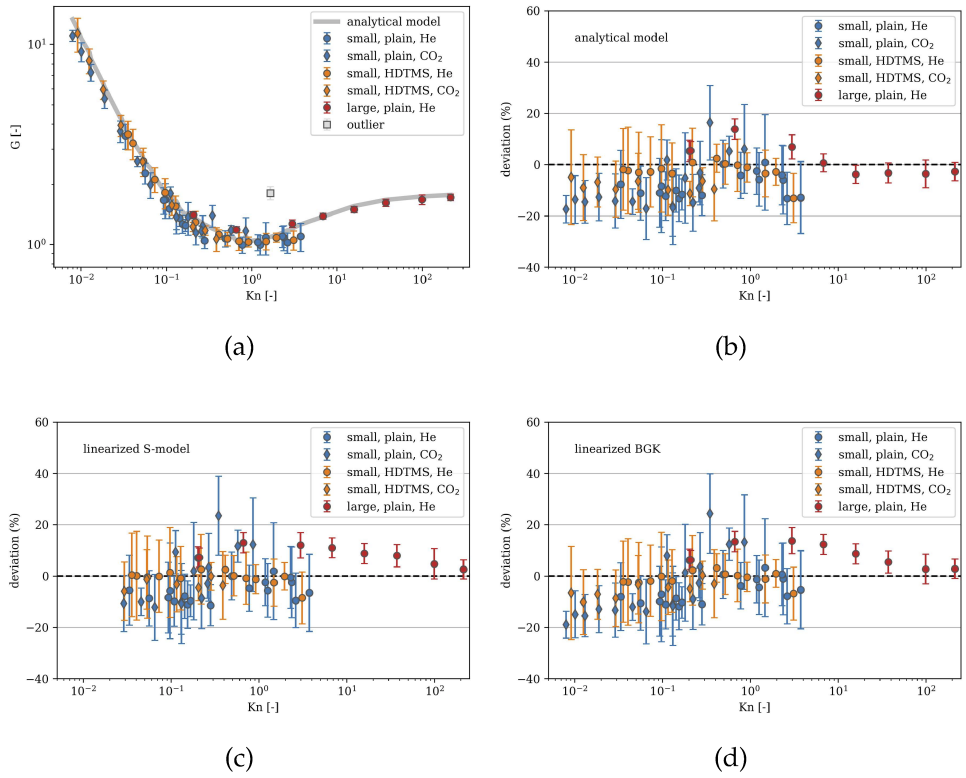

Figure 4.13: **(a)** Dimensionless mass flow rate obtained experimentally (symbols) and calculated from the analytical model [6] (line). The outlier in gray color is not included in the Plots (b)-(d). **(b)** Comparison of experiments to the analytical model. A negative value corresponds to an experimental value smaller than the analytical one. **(c)** Comparison of experiments to the numerical solution of the linearized S-model equation [112]. **(d)** Comparison of experiments to the numerical solution of the linearized BGK equation.

model and numerical solutions of both kinetic equations. All neighboring measurement points have overlapping measurement uncertainties, indicating an overall consistent result. All three models mostly lie within experimental error with deviations smaller than 20 % except for a single value.

To quantify the difference in mass flow rate between plain and functionalized channels, a t-test using unequal variances [113] is performed. The populations are the deviations between experiment and analytical model for plain and functionalized channels, respectively. The null hypothesis is that the populations have the same means. The populations include all gases and channels. The test results in a p-value of 0.303, showing that there is no significant difference in mass flow rate between plain and functionalized channels.

The analytical model introduced in section 3.3 is applied without any

modification or adaption to the experimental data acquired here. As discussed before, while the model uses a TMAC of 0.9 for the slip flow in rectangular channels, the actual TMAC should be 1 for all Knudsen numbers. The TMAC of 0.9 is attributed to a supposedly imperfect slip expression for rectangular channels. There seems to be a complicating influence of the more complex rectangular geometry. A strong evidence that this is indeed the case is that if the TMAC was originally 0.9 for plain channels, it should become 1 when HDTMS is applied to the channel surfaces. HDTMS would sterically prevent any specular reflection, for which an even surface is needed [39]. Because the mass flow does not change with functionalization, however, this means that the TMAC is 1 even for the plain channels. Both the calculations of the linearized S-model and BGK equations use a TMAC of 1, further strengthening this claim because of the good agreement with the experimental data and the analytical model.

4.6 One volume *versus* two volumes

As described in section 4.4.2, the methodology for calculating the uncertainty of experiments differ depending on whether both upstream and downstream volumes or only one volume is used. For the data acquired at the IUSTI laboratory, two independent data sets are produced, one for the upstream, one for the downstream volume. For the TRANSFLOW facility, the downstream volume is continuously evacuated, therefore only data for the upstream volume is available.

The great benefit of having two volumes is that this makes sure that the experiment is intrinsically valid. If there was any leakage or outgassing in the facility, this would result in a rise of pressure in both volumes, reducing the calculated mass flow in the upstream volume and enhancing it in the downstream volume, therefore resulting in a divergence of the theoretically same mass flow rates. This, in turn, results in a larger uncertainty because a larger threshold in the data fragment method would be necessary to find a sufficiently large area in the array.

That control instance is not available when using only one volume, because the mass flow rate of a single fragment is compared to the data *from the same data set*. This results in two challenges: first, because the mass flow rate of one fragment is compared to the mass flow rate of other fragments using other window starts, the initial pressure is not the same in both cases. Because of a different upstream pressure (and possibly a different downstream

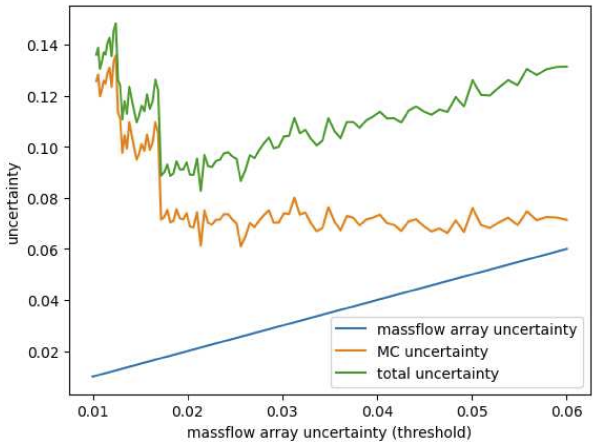

Figure 4.14: The sampling of thresholds with the two parts of the total uncertainty, only using the upstream pressure drop

pressure at the same time), this results in a different mass flow rate. Therefore, even with a totally valid experimental run having an optimal signal-to-noise ratio, there must be a threshold larger than zero to include enough data to have a 20 % area. The second challenge is that influences like leakage and outgassing affect the whole data set in the same way and is therefore not detectable using this method.

The first challenge should, in theory, increase the resulting uncertainty because of the changing mass flow rate with changing window start. The second challenge should decrease the uncertainty because influences like leakage and outgassing do not influence the result. To investigate this, the data fragment method is applied to the data acquired at the IUSTI laboratory only using the inlet volume. A threshold sampling of the same run as depicted in figure 4.12 is shown in figure 4.14.

The minimal uncertainty of the Monte Carlo simulations is reached for much lower thresholds. This results in a significantly lower total uncertainty, showing that the influence of leakage or outgassing is larger that the influence of a changing mass flow rate with time.

The same picture is painted in figure 4.15, where uncertainties of all runs are significantly smaller than those calculated with both upstream and downstream pressure information. Note that the TRANSFLOW results are, of course, the same, since they only use the upstream pressure anyway.

Two main conclusions can be drawn from figure 4.15: the models are not within the uncertainty of the data to the extent as when using both upstream and downstream pressures. This could lead to the interpretation that the models do not represent the underlying physical effects satisfyingly. The

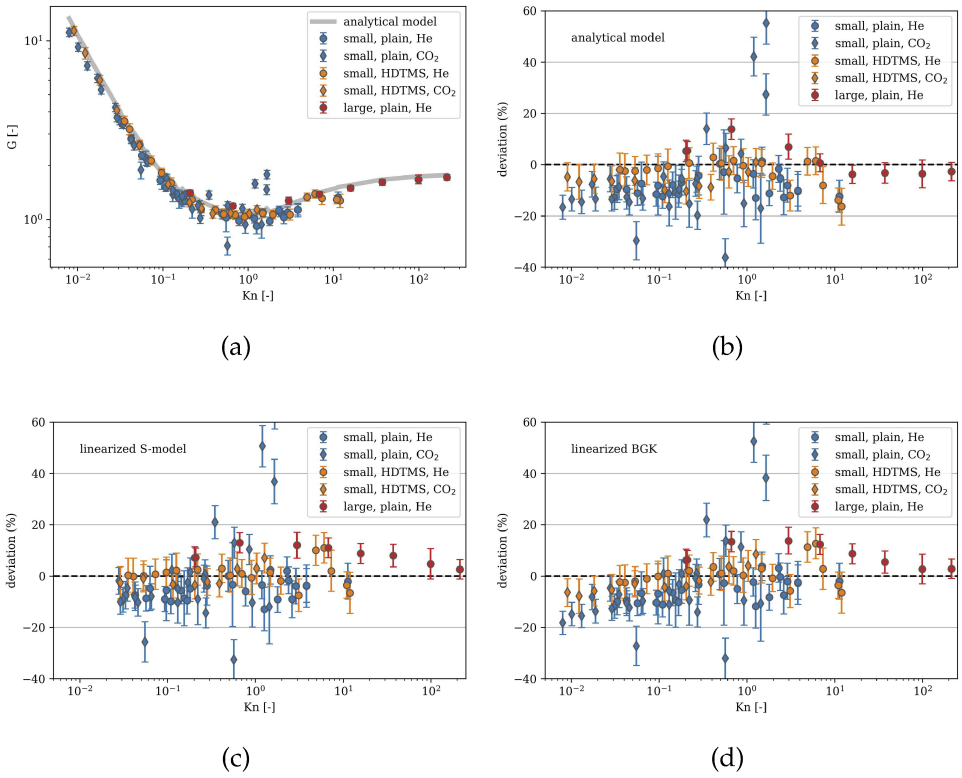

Figure 4.15: The results when only using the upstream pressure drop for the IUSTI data. **(a)** Dimensionless mass flow rate obtained experimentally (symbols) and calculated from the analytical model [6] (line). **(b)** Comparison of experiments to the analytical model. **(c)** Comparison of experiments to the numerical solution of the linearized S-model equation [112]. **(d)** Comparison of experiments to the numerical solution of the linearized BGK equation.

other aspect is that some obvious outliers are not detected, because their uncertainty stays below 20 %. Both these aspects are not valid, because they do not emerge from precise measurements but rather from an incomplete analysis of the available data.

Chapter 5

Conclusion

Modeling a system can have two goals - use the model to predict the outcome, and get a better understanding of underlying principles. Purely empirical models fall into the first category, while models based on physical foundations add the latter. The model presented in this thesis allows describing rarefied gas flows in a simple, analytical form. It not only allows to predict those gas flows outside the boundaries used to derive the model - its simple form makes it possible to develop an intuition about the processes involved.

This does not mean that it correctly describes the reality in an absolute way. It is, like all models, an approximation, which is not valid for all cases: in this work, only straight channels are considered - with circular and rectangular cross-sections at that. But in combination with the experimental data acquired in functionalized microchannels, it is possible to draw some general conclusions which may even exceed the scope of the model itself.

A central aspect is the importance of geometric scale. From a gas kinetics perspective, the scale of the channel should not have an influence on the dimensionless mass flow. This is indeed the case when considering surface interactions which can be described by the TMAC. But as soon as those surfaces are functionalized, effects arise which are not only dependent on the Knudsen number. The fact that in small geometries on the nanometer scale, the gas flow is strongly influenced by functionalization opposed to gas flow in the micrometer channels considered here shows that there must be an influence of the surface-to-volume ratio. This is an intuitive outcome when applying the same logic as with the surface diffusion, where the absolute influence is proportional to the available surface. But it is no trivial result by any means - for example, the pressure is lower in larger structures for the same Knudsen numbers, which could in turn influence the interaction with the surface functionalization. If such an effect is present, however, it is obscured by the surface-to-volume ratio influence.

A quite general result of this work is that technical surfaces are likely to have a TMAC of 1. The model uses a TMAC of 0.9 for the slip expression because of a potential imperfection of the slip expression. The slip flow regime is generally used to extract the TMAC which could explain the general misconception in the literature and results for the TMAC smaller than 1. A very clear indicator, however, is the data for the free molecular regime, which clearly does not represent any TMAC smaller than 1. The consequence of this is that there is potential for improvement for slip expressions for rectangular channels and, potentially, for more complex geometries.

This generalization of the slip expression would also be needed for a generalization of the whole model. If the generalization could be performed numerically, the superposition approach may be an option to approximate arbitrarily complex gas flows using very easy to solve equations, compared to established numerical methods.

Finally, the *data fragment method* proved to be a reliable way of analyzing rather noisy and unstable pressure drop data and could be adapted to different situations for extracting a subset of a data series fulfilling certain requirements not only by chance.

Appendix A

Supplementary materials

A.1 Knudsen numbers of technical applications

Adsorption materials: Pore sizes of 200 µm down to 0.1 nm. Large changes in pressure or temperature in swing-adsorption applications result in Knudsen numbers ranging from ∼0 to 10.

Catalyst: Pore diameter distribution: 12 – 80 nm. Mean free path of air at 1 atm: 70 nm. This results in Knudsen numbers of 0.9 to 6.

Space propulsion systems: Typical length scales of 1 – 10 cm. Due to the big pressure differences between ignition chamber and free space, the Knudsen numbers range from 0.1 up to 100.

A.2 CAD drawings

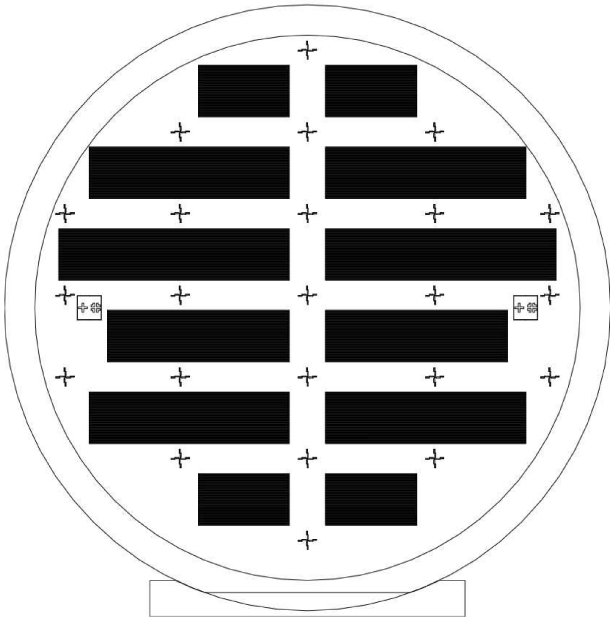

Figure A.1: CAD drawing of the small microchannels.

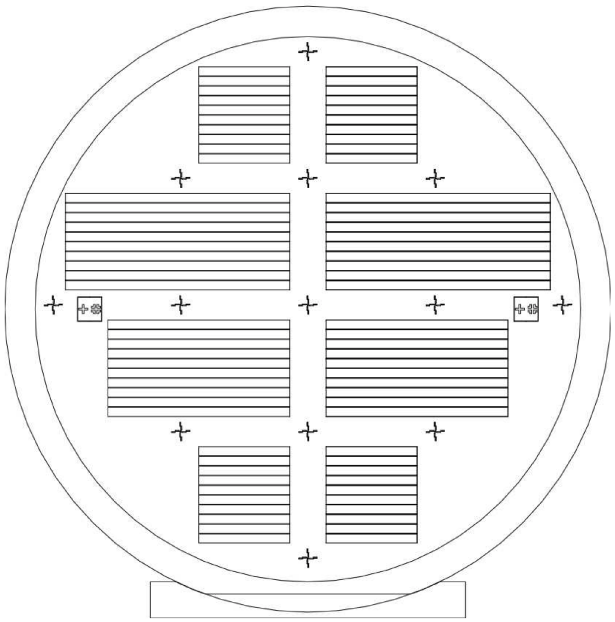

Figure A.2: CAD drawing of the large microchannels.

A.3 Data preparation

The pressure, measured in Volts, is converted to Pascal by these steps:

Preparation for TRANSFLOW data

1. Apply pressure sensor offset by subtracting the background measurement,
2. convert Volt to Pascal by using a simple linear relation specific to a pressure sensor,
3. apply the correction provided by a calibration certificate,
4. apply temperature compensation by using the ideal gas law to exclude any influences of temperature fluctuation.

Preparation for IUSTI data

1. Convert Volt to Pascal by using a simple linear relation specific to a pressure sensor,
2. apply a leakage correction using a previously performed leakage measurement

A.4 Leakage influences at IUSTI laboratory

`D2_CO2_1000_100_leakage_07-12-21`

- inlet sensor: 1000
- outlet sensor: 100
- $\dot{p}_1$: -5.915e-5 Pa/s
- $\dot{p}_2$: 3.561e-5 Pa/s
- used by:
  - `D2_CO2_1000_100_massflow_5k_1k_08-12-21`
  - `D2_CO2_1000_100_massflow_11k_2k_09-12-21`
  - `D2_CO2_1000_100_massflow_22k_4k_09-12-21`
  - `D2_CO2_1000_100_massflow2_11k_2k_09-12-21`

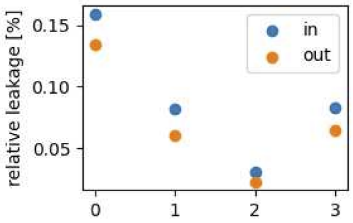

Figure A.3: Relative leakage of `D2_CO2_1000_100_leakage_07-12-21`

`D2_He_1000_100_leakage_10k_14-01-22`

- inlet sensor: 1000
- outlet sensor: 100
- $\dot{p}_1$: 0.0355 Pa/s
- $\dot{p}_2$: 0.00664 Pa/s
- used by:
  - `D2_He_1000_100_massflow_32k_12k_14-01-22`
  - `D2_He_1000_100_massflow_40k_11k_14-01-22`
  - `D2_He_1000_100_massflow_58k_11k_14-01-22`

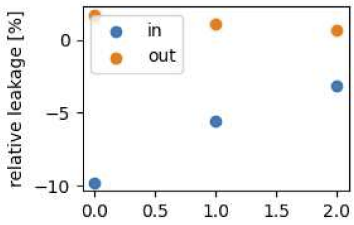

Figure A.4: Relative leakage of `D2_He_1000_100_leakage_10k_14-01-22`

`D2_He_100_100_leakage_1700_18-01-22`

- inlet sensor: 100
- outlet sensor: 100
- $\dot{p}_1$: 0.000945 Pa/s
- $\dot{p}_2$: 0.000973 Pa/s
- used by:
  - `D2_He_100_100_massflow_5200_1100_18-01-22`
  - `D2_He_100_100_massflow_6k_3k_18-01-22`
  - `D2_He_100_100_massflow_10k_5k_18-01-22`

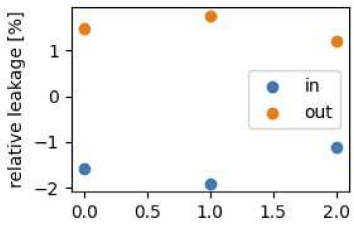

Figure A.5: Relative leakage of `D2_He_100_100_leakage_1700_18-01-22`

`D2_He_1000_1000_leakage_42k_08-02-22`

- inlet sensor: 1000
- outlet sensor: 1000
- $\dot{p}_1$: 0.0129 Pa/s
- $\dot{p}_2$: 0.00485 Pa/s

- used by:
  - D2_He_1000_1000_massflow_133k_90k_08-02-22
  - D2_He_1000_1000_massflow_83k_49k_08-02-22
  - D2_He_1000_1000_massflow_56k_25k_08-02-22

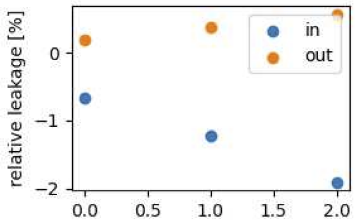

Figure A.6: Relative leakage of D2_He_1000_1000_leakage_42k_08-02-22

C2_He_100_100_leakage_700_18-03-22

- inlet sensor: 100
- outlet sensor: 100
- $\dot{p}_1$: 0.000861 Pa/s
- $\dot{p}_2$: 0.00115 Pa/s
- used by:
  - C2_He_100_100_massflow_12k_3k_18-03-22
  - C2_He_100_100_massflow_13k_5k_18-03-22
  - C2_He_100_100_massflow_6500_1600_18-03-22
  - C2_He_100_100_massflow_7900_2600_18-03-22
  - C2_He_100_100_massflow_1950_400_18-03-22
  - C2_He_100_100_massflow_3400_430_18-03-22
  - C2_He_100_100_massflow_4300_700_18-03-22

C2_CO2_100_100_leakage_14-03-22

- inlet sensor: 100
- outlet sensor: 100
- $\dot{p}_1$: 0.00192 Pa/s

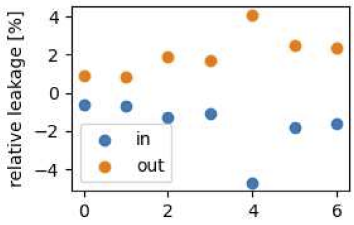

Figure A.7: Relative leakage of `C2_He_100_100_leakage_700_18-03-22`

- $\dot{p}_2$: 0.00217 Pa/s
- used by:
  - `C2_CO2_100_100_massflow_5k_1k_14-03-22`
  - `C2_CO2_100_100_massflow_6k_2k_14-03-22`
  - `C2_CO2_100_100_massflow_12k_3k_14-03-22`
  - `C2_CO2_100_100_massflow_12k_3k_14-03-22`

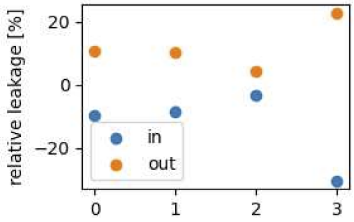

Figure A.8: Relative leakage of `C2_CO2_100_100_leakage_14-03-22`

Appendix B

Student's work

In this dissertation, no results of students' works are included.

Bibliography

[1] A. Montessori, P. Prestininzi, M. La Rocca, G. Falcucci, S. Succi, and E. Kaxiras. "Effects of Knudsen Diffusivity on the Effective Reactivity of Nanoporous Catalyst Media". *Journal of Computational Science* 17 (Nov. 2016), pp. 377–383. DOI: 10.1016/j.jocs.2016.04.006.

[2] C. White, C. Colombo, T. J. Scanlon, C. R. McInnes, and J. M. Reese. "Rarefied Gas Effects on the Aerodynamics of High Area-to-Mass Ratio Spacecraft in Orbit". *Advances in Space Research* 51.11 (June 2013), pp. 2112–2124. DOI: 10.1016/j.asr.2013.01.002.

[3] R. W. Baker. *Membrane Technology and Applications*. John Wiley and Sons Ltd, 2012. DOI: 10.1002/9781118359686.ch2.

[4] C.-M. Ho and Y.-C. Tai. "Micro-Electro-Mechanical-Systems (MEMS) and Fluid Flows". *Annual Review of Fluid Mechanics* 30.1 (Jan. 1998), pp. 579–612. DOI: 10.1146/annurev.fluid.30.1.579.

[5] W. Bauer, P. Rickmers, A. Kallenbach, S. Stappert, V. Wartemann, C. Hans-Joachim Merrem, R. Schwarz, M. Sagliano, J. T. Grundmann, A. Flock, T. Thiele, D. Kiehn, A. Bierig, J. Windelberg, E. Ksenik, T. Bruns, T. Ruhe, and H. Elsäßer. "DLR Reusability Flight Experiment ReFEx". *Acta Astronautica* 168 (Mar. 2020), pp. 57–68. DOI: 10.1016/j.actaastro.2019.11.034.

[6] S. Kunze, R. Groll, B. Besser, and J. Thöming. "Molecular Diameters of Rarefied Gases". *Scientific Reports* 12.1 (2022), p. 2057. DOI: 10.1038/s41598-022-05871-y.

[7] F. Sharipov. "Rarefied Gas Flow through a Long Rectangular Channel". *Journal of Vacuum Science & Technology A: Vacuum, Surfaces, and Films* 17.5 (1999), pp. 3062–3066. DOI: 10.1116/1.582006.

[8] R. S. Brodkey and H. C. Hershey. *Transport Phenomena - Volume 2*. Brodkey Publishing, 1988.

[9] G. Karniadakis, A. Beskok, and N. Aluru. *Microflows and Nanoflows*. Ed. by S. Antman, J. Marsden, and L. Sirovich. Vol. 29. Interdisciplinary Applied Mathematics. New York: Springer-Verlag, 2005. DOI: 10.1007/0-387-28676-4.

[10] A. Beskok, G. E. Karniadakis, and W. Trimmer. "Rarefaction and Compressibility Effects in Gas Microflows". *Journal of Fluids Engineering* 118.3 (1996), pp. 448–456. DOI: 10.1115/1.2817779.

[11] S. P. Sutera and R. Skalak. "The History of Poiseuille's Law". *Annual Review of Fluid Mechanics* 25.1 (Jan. 1993), pp. 1–20. DOI: 10.1146/annurev.fl.25.010193.000245.

[12] L. Boltzmann. *Vorlesungen Über Gastheorie: 1. Teil*. Deutsches Textarchiv, 1896.

[13] L. Boltzmann. *Vorlesungen Über Gastheorie: 2. Teil*. Deutsches Textarchiv, 1896.

[14] L. Boltzmann. *Lectures on Gas Theory*. Dover ed. New York: Dover Publications, 1995.

[15] C. Shen. *Rarefied Gas Dynamics - Fundamentals, Simulations and Micro Flows*. Springer Science + Business Media, 2005.

[16] C. Cercignani. "The Boltzmann Equation". In: *The Boltzmann Equation and Its Applications*. Vol. 67. New York, NY: Springer New York, 1988, pp. 40–103. DOI: 10.1007/978-1-4612-1039-9_2.

[17] P. L. Bhatnagar, E. P. Gross, and M. Krook. "A Model for Collision Processes in Gases. I. Small Amplitude Processes in Charged and Neutral One-Component Systems". *Physical Review* 94.3 (May 1954), pp. 511–525. DOI: 10.1103/PhysRev.94.511.

[18] M. Knudsen. "Die Gesetze Der Molekularströmung Und Der Inneren Reibungsströmung Der Gase Durch Röhren". *Annalen der Physik* 333.1 (1909), pp. 75–130. DOI: 10.1002/andp.19093330106.

[19] M. v Smoluchowski. "Zur Kinetischen Theorie Der Transpiration Und Diffusion Verdünnter Gase". *Annalen der Physik* 338.16 (1910), pp. 1559–1570. DOI: 10.1002/andp.19103381623.

[20] P. Clausing. "Über die Strömung sehr verdünnter Gase durch Röhren von beliebiger Länge". *Annalen der Physik* 404.8 (1932), pp. 961–989. DOI: 10.1002/andp.19324040804.

[21] L. M. Lund and A. S. Berman. "Flow and Self-Diffusion of Gases in Capillaries. Part I". *Journal of Applied Physics* 37.6 (1966), pp. 2489–2495. DOI: 10.1063/1.1708841.

[22] M. A. Gallis and J. R. Torczynski. "Direct Simulation Monte Carlo-based Expressions for the Gas Mass Flow Rate and Pressure Profile in a Microscale Tube". *Physics of Fluids* 24.1 (2012), p. 012005. DOI: 10.1063/1.3678337.

[23] Q. Lv, X. Liu, E. Wang, and S. Wang. "Analytical Solution to Predicting Gaseous Mass Flow Rates of Microchannels in a Wide Range of Knudsen Numbers". *Physical Review E* 88.1 (2013), p. 013007. DOI: 10.1103/physreve.88.013007.

[24] G. A. Bird. "Direct Simulation and the Boltzmann Equation". *Physics of Fluids* 13.11 (1970), p. 2676. DOI: 10.1063/1.1692849.

[25] D. Valougeorgis and J. R. Thomas. "Exact Numerical Results for Poiseuille and Thermal Creep Flow in a Cylindrical Tube". *Physics of Fluids* 29.2 (1986), p. 423. DOI: 10.1063/1.865725.

[26] S. K. Loyalka and S. A. Hamoodi. "Poiseuille Flow of a Rarefied Gas in a Cylindrical Tube: Solution of Linearized Boltzmann Equation". *Physics of Fluids A: Fluid Dynamics* 2.11 (Nov. 1990), pp. 2061–2065. DOI: 10.1063/1.857681.

[27] F. M. Sharipov and V. D. Seleznev. "Rarefied Gas Flow through a Long Tube at Any Pressure Ratio". *Journal of Vacuum Science & Technology A: Vacuum, Surfaces, and Films* 12.5 (1994), pp. 2933–2935. DOI: 10.1116/1.578969.

[28] E. Arkillic and K. Breuer. "Gaseous Flow in Small Channels". In: *3rd Shear Flow Conference*. Orlando,FL,U.S.A.: American Institute of Aeronautics and Astronautics, July 1993. DOI: 10.2514/6.1993-3270.

[29] J. C. Harley, Y. Huang, H. H. Bau, and J. N. Zemel. "Gas Flow in Micro-Channels". *Journal of Fluid Mechanics* 284 (Feb. 1995), pp. 257–274. DOI: 10.1017/S0022112095000358.

[30] T. Graham. "On the Absorption and Dialytic Separation of Gases by Colloid Septa". *Philosophical Transactions of the Royal Society of London* 156 (Dec. 1866), pp. 399–439. DOI: 10.1098/rstl.1866.0018.

[31] B. Besser, S. Kunze, M. Wilhelm, K. Rezwan, and J. Thöming. "Surface Functionalization of Mesoporous Membranes: Impact on Pore Structure and Gas Flow Mechanisms". *ACS Applied Materials & Interfaces* 12.35 (2020), pp. 39388–39396. DOI: 10.1021/acsami.0c08619.

[32] J. Maurer, P. Tabeling, P. Joseph, and H. Willaime. "Second-Order Slip Laws in Microchannels for Helium and Nitrogen". *Physics of Fluids* 15.9 (2003), pp. 2613–2621. DOI: 10.1063/1.1599355.

[33] J. C. Maxwell. "On Stresses in Rarified Gases Arising from Inequalities of Temperature". *Philosophical Transactions of the Royal Society of London* 170 (1879), pp. 231–256. DOI: 10.1098/rstl.1879.0067.

[34] I. A. Graur, P. Perrier, W. Ghozlani, and J. G. Méolans. "Measurements of Tangential Momentum Accommodation Coefficient for Various Gases in Plane Microchannel". *Physics of Fluids* 21.10 (2009), p. 102004. DOI: 10.1063/1.3253696.

[35] E. B. Arkilic, K. S. Breuer, and M. A. Schmidt. "Mass Flow and Tangential Momentum Accommodation in Silicon Micromachined Channels". *Journal of Fluid Mechanics* 437 (2001), pp. 29–43. DOI: 10.1017/s0022112001004128.

[36] T. Ewart, P. Perrier, I. Graur, and J. G. Méolans. "Tangential Momemtum Accommodation in Microtube". *Microfluidics and Nanofluidics* 3.6 (2007), pp. 689–695. DOI: 10.1007/s10404-007-0158-3.

[37] P. Perrier, I. A. Graur, T. Ewart, and J. G. Méolans. "Mass Flow Rate Measurements in Microtubes: From Hydrodynamic to near Free Molecular Regime". *Physics of Fluids* 23.4 (2011), p. 042004. DOI: 10.1063/1.3562948.

[38] A. Agrawal and S. V. Prabhu. "Survey on Measurement of Tangential Momentum Accommodation Coefficient". *Journal of Vacuum Science & Technology A: Vacuum, Surfaces, and Films* 26.4 (2008), pp. 634–645. DOI: 10.1116/1.2943641.

[39] A. Keerthi, A. K. Geim, A. Janardanan, A. P. Rooney, A. Esfandiar, S. Hu, S. A. Dar, I. V. Grigorieva, S. J. Haigh, F. C. Wang, and B. Radha. "Ballistic Molecular Transport through Two-Dimensional Channels". *Nature* 558.7710 (2018), pp. 420–424. DOI: 10.1038/s41586-018-0203-2.

[40] T. Engel. "A Molecular Beam Investigation of He, CO, and O2 Scattering from Pd(111)". *The Journal of Chemical Physics* 69.1 (1978), p. 373. DOI: 10.1063/1.436363.

[41] G. Ehrlich and K. Stolt. "Surface Diffusion". *Annual Review of Physical Chemistry* 31.1 (1980), pp. 603–637. DOI: 10.1146/annurev.pc.31.100180.003131.

[42] A. Kapoor, R. T. Yang, and C. Wong. "Surface Diffusion". *Catalysis Reviews* 31.1-2 (1989), pp. 129–214. DOI: 10.1080/01614948909351350.

[43] J.-H. Moon, Y.-J. Park, M.-B. Kim, S.-H. Hyun, and C.-H. Lee. "Permeation and Separation of a Carbon Dioxide/Nitrogen Mixture in a Methyltriethoxysilane Templating Silica/α-Alumina Composite Membrane". *Journal of Membrane Science* 250.1-2 (2005), pp. 195–205. DOI: 10.1016/j.memsci.2004.10.027.

[44] A. W. Thornton, T. Hilder, A. J. Hill, and J. M. Hill. "Predicting Gas Diffusion Regime within Pores of Different Size, Shape and Composition". *Journal of Membrane Science* 336.1-2 (2009), pp. 101–108. DOI: 10.1016/j.memsci.2009.03.019.

[45] I. Medveď and R. Černý. "Surface Diffusion in Porous Media: A Critical Review". *Microporous and Mesoporous Materials* 142.2-3 (2011), pp. 405–422. DOI: 10.1016/j.micromeso.2011.01.015.

[46] S.-T. Hwang and K. Kammermeyer. "Surface Diffusion in Microporous Media". *The Canadian Journal of Chemical Engineering* 44.2 (1966), pp. 82–89. DOI: 10.1002/cjce.5450440206.

[47] I. Langmuir. "The Adsorption of Gases on Plane Surfaces of Glass, Mica and Platinum". *Journal of the American Chemical Society* 40.9 (Sept. 1918), pp. 1361–1403. DOI: 10.1021/ja02242a004.

[48] D. Stoltenberg and A. Seidel-Morgenstern. "An Attempt to Alter the Gas Separation of Mesoporous Glass Membranes by Amine Modification". *Microporous and Mesoporous Materials* 154 (2012), pp. 148–152. DOI: 10.1016/j.micromeso.2011.11.013.

[49] S. Suzuki, S. B. Messaoud, A. Takagaki, T. Sugawara, R. Kikuchi, and S. T. Oyama. "Development of Inorganic–Organic Hybrid Membranes for Carbon Dioxide/Methane Separation". *Journal of Membrane Science* 471 (2014), pp. 402–411. DOI: 10.1016/j.memsci.2014.08.029.

[50] D. Wang, H. Shakeel, J. Lovette, G. W. Rice, J. R. Heflin, and M. Agah. "Highly Stable Surface Functionalization of Microgas Chromatography Columns Using Layer-by-Layer Self-Assembly of Silica Nanoparticles". *Analytical Chemistry* 85.17 (Sept. 2013), pp. 8135–8141. DOI: 10.1021/ac401080u.

[51] S. B. Messaoud, A. Takagaki, T. Sugawara, R. Kikuchi, and S. T. Oyama. "Alkylamine–Silica Hybrid Membranes for Carbon Dioxide/Methane Separation". *Journal of Membrane Science* 477 (Mar. 2015), pp. 161–171. DOI: 10.1016/j.memsci.2014.12.022.

[52] C. Leger, H. D. L. Lira, and R. Paterson. "Preparation and Properties of Surface Modified Ceramic Membranes. Part III. Gas Permeation of 5 Nm Alumina Membranes Modified by Trichloro-Octadecylsilane". *Journal of Membrane Science* 120.2 (1996), pp. 187–195. DOI: 10.1016/0376-7388(96)00143-3.

[53] M. Krogh. "The Diffusion of Gases through the Lungs of Man". *The Journal of Physiology* 49.4 (1915), pp. 271–300. DOI: 10.1113/jphysiol.1915.sp001710.

[54] V. I. Dybkov. "Reaction Diffusion in Heterogeneous Binary Systems". *Journal of Materials Science* 21.9 (1986), pp. 3078–3084. DOI: 10.1007/bf00553339.

[55] G. Falkovich. *Fluid Mechanics*. Cambridge University Press, 2018. DOI: 10.1017/9781316416600.

[56] A. Bondi. "Van Der Waals Volumes and Radii". *The Journal of Physical Chemistry* 68.3 (1964), pp. 441–451. DOI: 10.1021/j100785a001.

[57] S. S. Batsanov. "Van Der Waals Radii of Elements". *Inorganic Materials* 37.9 (2001), pp. 871–885. DOI: 10.1023/a:1011625728803.

[58] J. P. O'Connell and J. M. Haile. "Thermodynamics" (2005). DOI: 10.1017/cbo9780511840234.

[59] J. D. van der Waals. "Over De Continuiteit Van Den Gasen Vloeistoftoestand". PhD thesis. 1873.

[60] D. R. Lide. *CRC Handbook of Chemistry and Physics: A Ready-Reference Book of Chemical and Physical Data*. CRC Press, 1995.

[61] J. Jang and S. T. Wereley. "Pressure Distributions of Gaseous Slip Flow in Straight and Uniform Rectangular Microchannels". *Microfluidics and Nanofluidics* 1.1 (2004), pp. 41–51. DOI: 10.1007/s10404-004-0005-8.

[62] J. R. Welty, G. L. Rorrer, and D. G. Foster. *Fundamentals of Momentum, Heat, and Mass Transfer*. Hoboken, NJ: Wiley, 2015.

[63] S. Tison. "Experimental Data and Theoretical Modeling of Gas Flows through Metal Capillary Leaks". *Vacuum* 44.11-12 (1993), pp. 1171–1175. DOI: 10.1016/0042-207x(93)90342-8.

[64] S. K. Dadzie and H. Brenner. "Predicting Enhanced Mass Flow Rates in Gas Microchannels Using Nonkinetic Models". *Physical Review E* 86.3 (Sept. 2012), p. 036318. DOI: 10.1103/PhysRevE.86.036318.

[65] T. Veltzke and J. Thöming. "An Analytically Predictive Model for Moderately Rarefied Gas Flow". *Journal of Fluid Mechanics* 698 (2012), pp. 406–422. DOI: 10.1017/jfm.2012.98.

[66] T. Veltzke. "On Gaseous Microflows Under Isothermal Conditions". PhD thesis. 2013.

[67] R. Groll, S. Kunze, and B. Besser. "Correction of Second-Order Slip Condition for Higher Knudsen Numbers by Approximation of Free-Molecular Diffusion". *Physics of Fluids* 32.9 (2020), p. 092008. DOI: 10.1063/5.0021711.

[68] A. Beskok and G. E. Karniadakis. "A Model for Flows in Channels, Pipes and Ducts At Micro and Nano Scales". *Microscale Thermophysical Engineering* 3.1 (1999), pp. 43–77. DOI: 10.1080/108939599199864.

[69] V. K. Michalis, A. N. Kalarakis, E. D. Skouras, and V. N. Burganos. "Rarefaction Effects on Gas Viscosity in the Knudsen Transition Regime". *Microfluidics and Nanofluidics* 9.4-5 (2010), pp. 847–853. DOI: 10.1007/s10404-010-0606-3.

[70] W. Wagner. "A Convergence Proof for Bird's Direct Simulation Monte Carlo Method for the Boltzmann Equation". *Journal of Statistical Physics* 66.3-4 (Feb. 1992), pp. 1011–1044. DOI: 10.1007/BF01055714.

[71] E. M. Shakhov. "Generalization of the Krook Kinetic Relaxation Equation". *Fluid Dynamics* 3.5 (1972), pp. 95–96. DOI: 10.1007/BF01029546.

[72] S. Varoutis, S. Naris, V. Hauer, C. Day, and D. Valougeorgis. "Computational and Experimental Study of Gas Flows through Long Channels of Various Cross Sections in the Whole Range of the Knudsen Number". *Journal of Vacuum Science & Technology A: Vacuum, Surfaces, and Films* 27.1 (2009), pp. 89–100. DOI: 10.1116/1.3043463.

[73] L. B. Loeb. *The Kinetic Theory Of Gases*. New York And London: Mcgraw-Hill Book Company Inc., 1934.

[74] T. Ewart, P. Perrier, I. A. Graur, and J. G. Méolans. "Mass Flow Rate Measurements in a Microchannel, from Hydrodynamic to near Free Molecular Regimes". *Journal of Fluid Mechanics* 584 (2007), p. 337. DOI: 10.1017/s0022112007006374.

[75] K. K. Kammara, G. Malaikannan, and R. Kumar. "Molecular Dynamics Study of Gas–Surface Interactions in a Force-Driven Flow of Argon through a Rectangular Nanochannel". *Nanoscale and Microscale Thermophysical Engineering* 20.2 (2016), pp. 121–136. DOI: 10.1080/15567265.2016.1215364.

[76] A. Satoh. "Introduction to Practice of Molecular Simulation" (2011), pp. 29–47. DOI: 10.1016/b978-0-12-385148-2.00002-1.

[77] R. S. Brodkey and H. C. Hershey. *Transport Phenomena - Volume 1*. Brodkey Publishing, 1988.

[78] W. G. Pollard and R. D. Present. "On Gaseous Self-Diffusion in Long Capillary Tubes". *Physical Review* 73.7 (1948), pp. 762–774. DOI: 10.1103/physrev.73.762.

[79] S. Geisser. *Predictive Inference*. CRC Press, 2017.

[80] A. Rohatgi. *Webplotdigitizer: Version 4.6*. 2022.

[81] S. Alvarez. "A Cartography of the van Der Waals Territories". *Dalton Transactions* 42.24 (2013), p. 8617. DOI: 10.1039/c3dt50599e.

[82] S. Kunze, P. Perrier, R. Groll, B. Besser, S. Varoutis, A. Lüttge, I. Graur, and J. Thöming. "Rarefied Gas Flow in Functionalized Microchannels" (2023). DOI: 10.48550/ARXIV.2301.12575.

[83] S. Colin. "Rarefaction and Compressibility Effects on Steady and Transient Gas Flows in Microchannels". *Microfluidics and Nanofluidics* 1.3 (2005), pp. 268–279. DOI: 10.1007/s10404-004-0002-y.

[84] H. Yamaguchi, T. Hanawa, O. Yamamoto, Y. Matsuda, Y. Egami, and T. Niimi. "Experimental Measurement on Tangential Momentum Accommodation Coefficient in a Single Microtube". *Microfluidics and Nanofluidics* 11.1 (2011), pp. 57–64. DOI: 10.1007/s10404-011-0773-x.

[85] T. Ewart, P. Perrier, I. Graur, and J. G. Méolans. "Mass Flow Rate Measurements in Gas Micro Flows". *Experiments in Fluids* 41.3 (2006), pp. 487–498. DOI: 10.1007/s00348-006-0176-z.

[86] E. Arkilic, M. Schmidt, and K. Breuer. "Gaseous Slip Flow in Long Microchannels". *Journal of Microelectromechanical Systems* 6.2 (1997), pp. 167–178. DOI: 10.1109/84.585795.

[87] S. Colin, P. Lalonde, and R. Caen. "Validation of a Second-Order Slip Flow Model in Rectangular Microchannels". *Heat Transfer Engineering* 25.3 (Apr. 2004), pp. 23–30. DOI: 10.1080/01457630490280047.

[88] A. K. Sreekanth. "Transition Flow through Short Circular Tubes". *Physics of Fluids* 8.11 (1965), p. 1951. DOI: 10.1063/1.1761142.

[89] M. Hadj-Nacer, P. Perrier, J. G. Méolans, I. Graur, and M. Wüest. "Experimental Study of the Gas Flows through Channels with Circular Cross Sections". *Journal of Physics: Conference Series* 362.1 (2012), p. 012025. DOI: 10.1088/1742-6596/362/1/012025.

[90] J. Pitakarnnop, S. Varoutis, D. Valougeorgis, S. Geoffroy, L. Baldas, and S. Colin. "A Novel Experimental Setup for Gas Microflows". *Microfluidics and Nanofluidics* 8.1 (2010), pp. 57–72. DOI: 10.1007/s10404-009-0447-0.

[91] G. P. Brown, A. DiNardo, G. K. Cheng, and T. K. Sherwood. "The Flow of Gases in Pipes at Low Pressures". *Journal of Applied Physics* 17.10 (Oct. 1946), pp. 802–813. DOI: 10.1063/1.1707647.

[92] B. T. Porodnov, P. E. Suetin, S. F. Borisov, and V. D. Akinshin. "Experimental Investigation of Rarefied Gas Flow in Different Channels". *Journal of Fluid Mechanics* 64.3 (1974), pp. 417–438. DOI: 10.1017/s0022112074002485.

[93] L. Marino. "Experiments on Rarefied Gas Flows through Tubes". *Microfluidics and Nanofluidics* 6.1 (2009), pp. 109–119. DOI: 10.1007/s10404-008-0311-7.

[94] A. E. Velasco, S. G. Friedman, M. Pevarnik, Z. S. Siwy, and P. Taborek. "Pressure-Driven Flow through a Single Nanopore". *Physical Review E* 86.2 (2012), p. 025302. DOI: 10.1103/physreve.86.025302.

[95] M. H. Hadj Nacer, I. Graur, and P. Perrier. "Mass Flow Measurement through Rectangular Microchannel from Hydrodynamic to near Free Molecular Regimes". *La Houille Blanche* 4 (2011), pp. 49–54. DOI: 10.1051/lhb/2011040.

[96] J. M. Anderson, M. W. Moorman, J. R. Brown, J. M. Hochrein, S. M. Thornberg, K. E. Achyuthan, M. A. Gallis, J. R. Torczynski, T. Khraishi, and R. P. Manginell. "Isothermal Mass Flow Measurements in Microfabricated Rectangular Channels over a Very Wide Knudsen Range". *Journal of Micromechanics and Microengineering* 24.5 (2014), p. 055013. DOI: 10.1088/0960-1317/24/5/055013.

[97] M. Bergoglio, D. Mari, J. Chen, H. S. H. Mohand, S. Colin, and C. Barrot. "Experimental and Computational Study of Gas Flow Delivered by a Rectangular Microchannels Leak". *Measurement* 73 (2015), pp. 551–562. DOI: 10.1016/j.measurement.2015.06.011.

[98] S. Franssila. *Introduction to Microfabrication*. 2010.

[99] A. Lüttge, E. W. Bolton, and A. Lasaga. "An Interferometric Study of the Dissolution Kinetics of Anorthite; the Role of Reactive Surface Area". *American Journal of Science* 299.7-9 (Nov. 1999), pp. 652–678. DOI: 10.2475/ajs.299.7-9.652.

[100] R. S. Arvidson, C. Fischer, D. S. Sawyer, G. D. Scott, D. Natelson, and A. Lüttge. "Lateral Resolution Enhancement of Vertical Scanning Interferometry by Sub-Pixel Sampling". *Microscopy and Microanalysis* 20.1 (Feb. 2014), pp. 90–98. DOI: 10.1017/S1431927613013822.

[101] F. Zhang, K. Sautter, A. M. Larsen, D. A. Findley, R. C. Davis, H. Samha, and M. R. Linford. "Chemical Vapor Deposition of Three Aminosilanes on Silicon Dioxide: Surface Characterization, Stability, Effects of Silane Concentration, and Cyanine Dye Adsorption". *Langmuir* 26.18 (2010), pp. 14648–14654. DOI: 10.1021/la102447y.

[102] S. J. Khatib and S. T. Oyama. "Silica Membranes for Hydrogen Separation Prepared by Chemical Vapor Deposition (CVD)". *Separation and Purification Technology* 111 (June 2013), pp. 20–42. DOI: 10.1016/j.seppur.2013.03.032.

[103] G. T. Hermanson. "Silane Coupling Agents". In: *Bioconjugate Techniques*. Elsevier, 2013, pp. 535–548. DOI: 10.1016/B978-0-12-382239-0.00013-3.

[104] C. A. Schneider, W. S. Rasband, and K. W. Eliceiri. "NIH Image to ImageJ: 25 Years of Image Analysis". *Nature Methods* 9.7 (2012), pp. 671–675. DOI: 10.1038/nmeth.2089.

[105] S. Varoutis, T. Giegerich, V. Hauer, and C. Day. "TRANSFLOW: An Experimental Facility for Vacuum Gas Flows". *Journal of Physics: Conference Series* 362.1 (2012), p. 012027. DOI: 10.1088/1742-6596/362/1/012027.

[106] R. Brancher, M. V. Johansson, P. Perrier, and I. Graur. "Measurements of Pressure Gradient and Temperature Gradient Driven Flows in a Rectangular Channel". *Journal of Fluid Mechanics* 923 (2021), A35. DOI: 10.1017/jfm.2021.586.

[107] M. R. Cardenas, I. Graur, P. Perrier, and J. G. Meolans. "Thermal Transpiration Flow: A Circular Cross-Section Microtube Submitted to a Temperature Gradient". *Physics of Fluids* 23.3 (2011), p. 031702. DOI: 10.1063/1.3561744.

[108] M. Rojas-Cárdenas, E. Silva, M.-T. Ho, C. J. Deschamps, and I. Graur. "Time-Dependent Methodology for Non-Stationary Mass Flow Rate Measurements in a Long Micro-Tube". *Microfluidics and Nanofluidics* 21.5 (2017), p. 86. DOI: 10.1007/s10404-017-1920-9.

[109] B. Illowsky and S. L. Dean. *Introductory Statistics*. Revision ST-2013-002(03/18)-LC. Houston, Texas: OpenStax, Rice University, 2018.

[110] C. E. Papadopoulos and H. Yeung. "Uncertainty Estimation and Monte Carlo Simulation Method". *Flow Measurement and Instrumentation* 12.4 (Aug. 2001), pp. 291–298. DOI: 10.1016/S0955-5986(01)00015-2.

[111] E. O. Lebigot. *Uncertainties: A Python Package for Calculations with Uncertainties*.

[112] I. Graur and M. Ho. "Rarefied Gas Flow through a Long Rectangular Channel of Variable Cross Section". *Vacuum* 101 (2014), pp. 328–332. DOI: 10.1016/j.vacuum.2013.07.047.

[113] B. L. Welch. "The Generalization of 'Student's' Problem When Several Different Population Variances Are Involved". *Biometrika* 34.1-2 (1947), pp. 28–35. DOI: 10.1093/biomet/34.1-2.28.

Eigenständigkeitserklärung

Hiermit erkläre ich, Simon Kunze, dass die vorliegende Dissertation mit dem Titel "Rarefied Gases and Functionalized Surfaces" gemäß §5 der Promotionsordnung des FB4 der Universität Bremen von mir ohne unerlaubte fremde Hilfe angefertigt worden ist.
Ich bestätige, dass ich keine anderen als die von mir angegebenen Quellen und Hilfsmittel benutzt habe.
Darüber hinaus versichere ich, dass ich die den benutzten Werken wörtlich oder inhaltlich entnommenen Stellen als solche kenntlich gemacht habe.
Ich bestätige, dass meine vorliegende Arbeit nach den geltenden Prinzipien der guten wissenschaftlichen Praxis der Universität Bremen und der Deutschen Forschungsgemeinschaft verfasst ist.

Ort, Datum Unterschrift